REVIEW ARTICLE - SOLID EARTH SCIENCES

Inference of fracturing zones and degrees of fluid content in the Las Tres Virgenes volcanic complex based on an analysis of seismic anisotropy

Francisco Chacón-Hernández[1] · Jose Oscar Campos-Enríquez[1] · Francisco Ramón Zúñiga[2] · Javier Lermo-Samaniego[3]

Abstract

Anisotropy strength in the Tres Vírgenes Volcanic Complex, Baja California Sur, Mexico, is analyzed employing 558 seismic events collected from 2009 to 2013. It was possible to delineate zones and volumes with the highest fracture densities, which are mainly located between the El Viejo and El Azufre volcanoes and around the La Reforma–El Azufre fault system, near some other mapped faults in the area (e.g., El Azufre, El Partido, El Volcán, El Viejo 1, and El Viejo 2 faults); likewise toward the La Virgen volcano and around the La Virgen-El Campamento and El Volcán faults. Individual delay times reached values of up to 0.16 s and an anisotropy percentage of up to 10.3%, with a pervasive anisotropy observed from at least a hypocentral distance of 3.5 km. High fracturing levels are observed from a depth of 7.0 km. Differences between splitting delays and the dominant frequency peaks obtained from the fast S phases allowed considering fracture systems with different degrees of fluid contents. Fractures with minor fluid contents were assumed for delay times higher than 0.03 s with lower dominant frequency peaks (< 1.0 Hz). Higher concentrations of fluid inclusions were assumed for splitting delays higher than 0.03 s but with larger dominant frequency peaks (> 1.0 Hz). Fractures systems chemically sealed or impermeable sealing caps were assumed for low splitting delays (< 0.02 s) with low dominant frequencies (< 1.0 Hz). These different fracture systems seem to be observed at least from 5- to 6-km depth intervals. Likewise, an analysis of the fast polarization directions with respect to different depth ranges (spanning from 3.0 to 8.0 km) has allowed observations of a strong NW–SE regional fracture system accompanied by minor NE–SW fracture systems. However, noteworthy variations from NW–SE to NE–SW, N–S, and E–W in fast polarization directions in rose diagrams have been preferentially observed for those seismic events deeper than 4–5 and 5–6 km in some areas, which could be indicating the location of magmatic bodies that probably caused the reorientation on fracture systems by changes in the local stress field. These magmatic bodies might be supported by a decrease in the dominant frequency peaks (lower than 1.0 Hz), percentage of anisotropy (from 0.1 to 2.5%), and S-wave velocities (from 1.0 to 2.7 km/s), which seem to be located from the 4.0-km depth but more concentrated from the 5–6-km depth interval.

Keywords Percentage of anisotropy · Shear-wave splitting delays · Fracturing · Fast shear waves · Dominant frequency peaks · The Tres Vírgenes volcanic complex

---

✉ Francisco Chacón-Hernández
  fcochaconsalemj@gmail.com

1 Instituto de Geofísica, Universidad Nacional Autónoma de México, 04510 Mexico City, CDMX, Mexico

2 Centro de Geociencias, Universidad Nacional Autónoma de México, 76230 Juriquilla, QRO, Mexico

3 Instituto de Ingeniería, Universidad Nacional Autónoma de México, 04510 Mexico City, CDMX, Mexico

Introduction

The shear-wave splitting phenomenon has been observed in many volcanic (e.g., Miller and Savage 2001; Roman et al. 2011; Baird et al. 2015) and geothermal areas (e.g., Zúñiga et al. 1995; Lou et al. 1997; Tang et al. 2005; Mroczek et al. 2020), whose corresponding studies have helped to show preferential structural alignments and fracture densities. The preferential structural alignments produce splitting of the shear wavefield into two orthogonally polarized phases with different velocities, the fast shear-wave phase S_1 and

the slow shear-wave phase S_2, a phenomenon also known as seismic birefringence. In the case of crack-controlled anisotropy, S_2 is perpendicular to the crack planes, while S_1 is polarized parallel to the crack plane which tends to point along the orientation of the principal horizontal stresses. This parameter is also known as the fast polarization direction parameter ϕ. The difference in arrival time between both phases is proportional to the magnitude of anisotropy or the integrated effect of anisotropy along the travel path (Savage et al. 2010), which is known as the delay time parameter δt. The estimation of both birefringence parameters forms the basis of the shear-wave splitting technique (SWS). In this study, the anisotropy percentage is particularly assumed to be an indicator of fracturing.

Volcanic areas have been considered as strategic environments due to their energetic potential by hosting geothermal fluids, where fractured rock volumes constitute the main target in geothermal exploration. Within this context, a good structural characterization of volcanic areas represents a challenge since they represent complex systems, consisting of both heterogeneous and anisotropic structures that evolve. Usually, they are influenced and affected by phenomena and dynamic processes, such as migrations of magmatic bodies, dyke pressurization, hydrothermalism, or meteoric fluids, producing changes in the local stress fields with alterations in the anisotropy strength (Baird et al. 2015). Furthermore, geothermal energy operations add an effect generated by injection/production activities that might enhance or affect the interaction between deeper or shallower crack systems, modifying the internal geometry (Sayers and Schutjens 2007) with cracks opening and closing (Mroczek et al. 2020). Usually, geothermal operations generate deformation mechanisms, cement breakage at grain contacts, grain sliding, and rotation (Schutjens et al. 2004), with tension and compression changes in the surrounding rock connected to the reservoir (Sayers and Schutjens 2007). These mechanisms lead to a combination of elastic and inelastic deformation processes (Sayers and Schutjens 2007) with changes in the rock volume by the flow rate out of or into the reservoir (Vasco et al. 2008). As a part of these geothermal operations, seismicity has been observed with time delays (Tosha et al. 1998), located far away (McGarr et al. 2002; Ellsworth 2013) and at greater depths of the injection zone, due to readjustment of the surrounding internal structures (Rubinstein and Mahani 2015).

These variations in space and time of seismic events have influenced the results of the ϕ and δt parameters (Johnson et al. 2011; Chacón-Hernández et al. 2021a), especially when several anisotropic sources contribute to the overall anisotropy. For example, crystals and mineral alignments (inherent properties of the rocks) can differ from a specific orientation of a fracture system (Kendall et al. 2007) or from the orientations of a group of fracture systems (Liu

et al. 1993; Erten et al. 2001). Similarly, some processes occurring in volcanic and geothermal environments, such as changes in pore-fluid pressure by injection procedures (Angerer et al. 2002) or by movement of magmatic bodies (Baird et al. 2015; Maher and Kendall 2018), could complicate the anisotropic analysis due to modifications in the geological structures. Likewise, hydrothermal systems can modify the rock volume (Teklemariam et al. 1996) and deform volcanic structures (e.g., at Aluto volcano, Nowacki et al. 2018). To avoid as much as possible anisotropic sources that could affect the anisotropic measurement, seismic information from a more restricted area can be considered to obtain an anisotropic signal freer from some influences and effects. For example, Gledhill et al. (1991) correlated local faults with more stable fast polarization directions when the analysis was limited to a minor area, in contrast to what was observed at other stations when data from a broader zone were included. When a broader area is analyzed, the birefringence parameters may show more regional influences, with a mean fast polarization direction parallel or sub-parallel to the maximum compression direction [e.g., Las Tres Vírgenes Volcanic Complex, Chacón-Hernández et al. 2021b], but also perpendicular [e.g., Mount Ruapehu, Miller and Savage 2001; Los Humeros Geothermal Field Chacón-Hernández et al. 2021a].

Different behaviors between the birefringence parameters (ϕ and δt), seismic wave velocities, and seismic frequency ranges have allowed studying those phenomena and dynamic processes mentioned above. For instance, when a medium contains fractures as main anisotropic structure, the anisotropy tends to become dependent on seismic frequency, with the fracture sizes (e.g., fracture connectivity) determining the behavior of this dependence (Rial et al. 2005) (e.g., the dominant frequencies drop for increases in δt or larger fracture sizes, Elkibbi 2004). From regional analyses, Marson-Pidgeon and Savage (1997) also observed a frequency-dependent anisotropy, with increasing δt values (from 1.0 to 4.0 s) for a lower dominant frequency range (from 0.05 to 0.2 Hz) and inversely. This shows how structural alignment influences seismic frequency ranges, but what happens if different types of fluids (e.g., vapor, liquid, magmatic, or mixtures of them) flow through these structures?

It has been observed that splitting times are induced by the different types of fluids and their contents, whose analysis is not always simple. In volcanic zones, increases in the percentage of anisotropy, as well as variations in ϕ and δt have been observed when geothermal procedures are carried out due to stimulation by hydraulic fracturing (e.g., Vlahovic et al. 2002; Rial et al. 2005; Mroczek et al. 2020). Gerst and Savage (2004) observed in a study of repressurization of magmatic fluids, higher anisotropy values ($> 5\%$) for typical frequency ranges of 4 Hz, where the deeper seismic events analyzed always presented lower frequency

ranges than the shallower ones. From local and regional events (SKS events), Audoine and Savage (2004) observed a frequency-dependent anisotropy, finding high splitting time values ($\delta t = 2.5 \pm 0.2$ s) for lower dominant frequencies (~ 0.0625 Hz), where the influence of fluid-filled cracks was considered as an important effect. Savage et al. (1990) observed for low dominant frequencies, shear-wave velocities of 3.3 km/s along with anisotropy from 0.18 to 4.3%, where fluid-filled cracks and microcrack were also considered as possible anisotropic causes. High S-wave attenuations and lower dominant frequencies have been observed when seismic waves pass through zones where the magma is molten or partially molten (e.g., Latter 1981; Gerst and Savage 2004; Vanorio et al. 2005). Likewise, non-permeable pathways and chemically sealed fractures have also been considered for reduced splitting times (Vlahovic et al. 2002).

Equivalent-medium theories have been used to model the elastic response of fractured rocks, assuming fractures as rotationally invariant 'penny-shaped' cracks. In such models, frequency-dependent anisotropy has also been observed by the influence of the alignment of inhomogeneities (e.g., fractures, fine layers, or fluid flow in porous rocks with micro-cracks and macro-fractures, Liu et al. 2003), also with decreases in δt and anisotropy as frequency ranges increases (e.g., Chesnokov et al. 2001; Liu et al. 2003). Chapman (2003) showed that larger fractures can introduce additional dispersion at lower frequency ranges, where anisotropy decreases (from 8 to 4%) as frequency increases (from 0.5 to 3.5 Hz). Fluid inclusions in fractures have also been considered as an important feature that affects the seismic frequencies and significantly the anisotropy (Thomsen 1995). Liu et al. (2000) and Chapman et al. (2003) have evidenced this sensitivity with variations on the seismic frequency ranges and elastic wave velocities. In sonic and ultrasonic laboratory measurements, these circumstances are observed for different types of fluids, such as oil, gas, and brine (e.g., based on the squirt-flow model, Maultzsch et al. 2003; Chapman et al. 2003). These analyses showed how gas inclusions in fractures generate lower compressional velocities than oil and brine at lower log frequencies (~ < 2 Hz) (i.e., at higher percentage of anisotropy), but higher compressional velocities at higher log frequencies (> 3 Hz, Chapman et al. 2003) (i.e., at lower percentage of anisotropy). Meanwhile, oil presented higher compressional velocities than brine at those lower log frequencies, but similar at higher log frequencies (Chapman et al. 2003).

From seismic exploration studies, SWS parameters have been observed to be sensitive to fractured rocks and fluid-filled fractures (e.g., gas into vertically fractured rock decreases slow shear-wave velocities and frequency content (< 12 Hz), van Der Kolk et al. 2001; Kozlov 2004). Shear-wave splittings have been observed to be higher for gas-filled than for liquid-filled fractures (van Der Kolk

et al. 2001). Stratifications also tend to generate changes in the seismic frequencies (e.g., Werner and Shapiro 1999), where increases and decreases in the frequency content are a function of permeability (Van der Kolk et al. 2001; Kozlov 2007). Likewise, the level of anisotropic arrangement has been considered as an influential factor in the frequency ranges. Lower dominant frequency ranges have been linked to fracture alignments presenting directions to the main fracture groups (Liu et al. 2003) or when they are more organized (Maultzsch et al. 2003). Nonetheless, increases in dominant frequencies may be observed when the anisotropic arrangements decrease (Marson-Pidgeon y Savage 1997).

The Tres Vírgenes Volcanic Complex (TVVC) constitutes a heterogeneous and anisotropic environment, whose tectonic background has been strongly modeled by the opening of the Gulf of California. Within the TVVC area, the Tres Vírgenes Geothermal Field (TVGF) has been in operation since the 1980's, whose effects on the shallower geology have been documented by numerous geological, geochemical, and geophysical studies (e.g., Campos-Enríquez 1992; López-Hernández et al. 1995; Romo et al. 2000; Wong et al. 2001; Lermo et al. 2010; Prol-Ledesma et al. 2016; Avellán et al. 2018, among others). Here, in this work, the SWS technique is used to analyze 558 seismic waveforms collected from 2009 to 2013, whose splitting parameters allowed defining those zones and pathways with the highest fracture densities in the TVVC, mainly linked in this work with the percentage of anisotropy, as well as the depths where pervasive anisotropy and high fracturing begins. Furthermore, possible effects of different degrees of fluid content in fracture systems, sealed fracture systems, and magmatic phenomena were also analyzed from the behavior of the dominant frequency peaks, S-wave velocities, anisotropy, and splitting delays. This was done by restricting the selection of seismic events to smaller study areas around the seismic stations (e.g., < 0.035° in latitude and longitude), and considering only those anisotropic signals with angles of incidence less than 45° to avoid the distortion in the incoming wave, influences of converted phases, and alterations in the splitting measurements as recommended by Evans (1984) and Booth and Crampin (1985).

General geology

The tectonic interaction between the Pacific and North American plates has structurally affected the Baja California Peninsula (BC) (inset showing the study area, Fig. 1). The interaction between these tectonic plates, along the Pacific coast of Mexico and the southwestern USA, produced Cenozoic magmatism since 25 Ma (Atwater 1989; Stock and Hodges 1989). At about 12.5 Ma, the Farallon paleo-plate stopped subduction beneath the Pacific and North American

Fig. 1 Inset showing the study area (in the black square) in the central eastern of the Baja California Peninsula (BC). The TVVC comprises the El Viejo (EVV), El Azufre (EAV), and La Virgen (LVV) volcanoes marked with black stars. LVF: Las Viboras Fault; EV1: El Viejo 1 Fault; EV2: El Viejo 2 Fault; EV: El Volcán Fault; SBR: Santa Rosalia Basin; SLR: Santa Lucia Range; SFR: San Francisco Range; EAC: El Aguajito Caldera; LRC: La Reforma Caldera
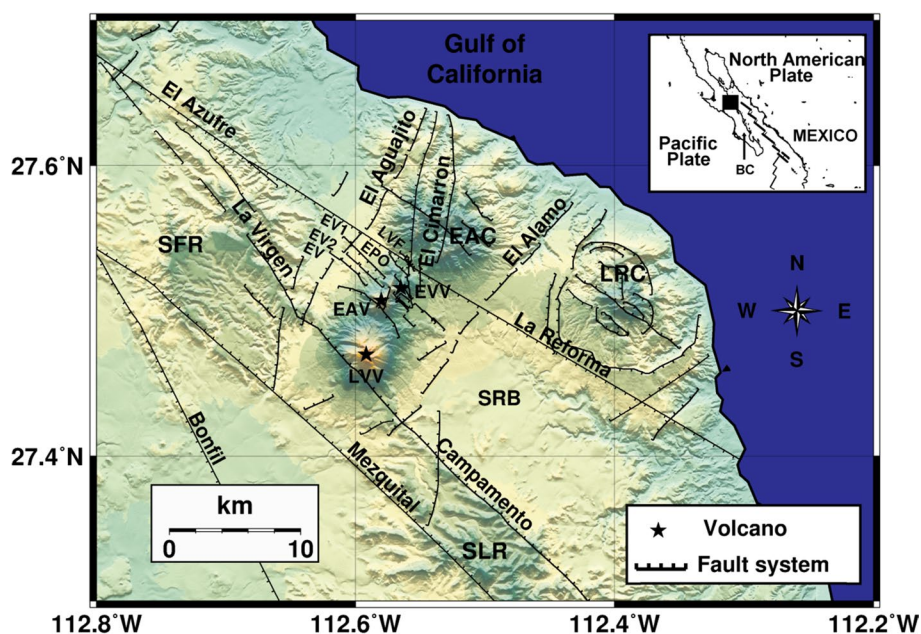
plates and started the opening of the Gulf of California with an N–NW oblique-strike-slip movement (Stock and Hodges 1989; Lonsdale 1991). Subsequently, the tectonism was followed and controlled by the deformation system related to the opening of the Gulf of California (Conly et al. 2005). This deformation system was characterized by an NW compressive stress field sub-parallel to the main rift margin faults with an E–W and E–NE extensional field, attributed to both local and regional tectonic processes (Bonini et al. 2019). In the Pliocene, an extensive deformation produced a set of normal faults and tilted blocks with preferential directions NW–SE, N–S, and NE–SW (Stock and Hodges 1989; Garduño-Monroy et al. 1993), as well as N–S trending fault systems (Coletta and Angelier 1981).

In the Pliocene–Quaternary, post-subduction magmatism took place with the ascent of magmatic bodies, which gave rise to the El Aguajito Caldera (EAC) and the La Reforma Caldera (LRC) (Garduño-Monroy et al. 1993; Demant 1981, 1984). On these post-subduction, volcanic rocks were emplaced the El Viejo (EVV), El Azufre (EAV), and La Virgen (LVV) volcanoes following the southwestern continuation of the NE–SW Cimarrón fault that crosses the EAC (e.g., Avellán et al. 2018). These three volcanoes form the so-called Tres Vírgenes Volcanic Complex (TVVC) (Gastil et al. 1975, 1979; Sawlan 1981), located in the northwestern portion of the Santa Rosalia basin (SRB) (Fig. 1), which is a Plio–Quaternary depression with an NW–SE trend (Demant 1981). The evolution of the TVVC is marked by periods of erosion and volcanic quiescence (López-Hernández et al. 1995).

In the TVVC area, regional NW–SE faults have been observed, whose origin has been associated with the Gulf of California opening (Garduño-Monroy et al. 1993; Macias-Vásquez and Jiménez-Salgado 2012). Fault systems, such as Mezquital, Bonfil, and Campamento correspond to normal faults with right-lateral components (e.g., Garduño-Monroy et al. 1993; Macias-Vásquez and Jiménez-Salgado 2012), which are located to the northwest and southwest of the TVVC (Fig. 1). The Mezquital fault bounds to the west the San Francisco Range (SFR), while the Campamento Fault limits to the east of the Santa Lucia Range (SLR). Local normal faulting has also been mapped (e.g., El Azufre, El Partido (EPO), El Viejo 1 (EV1), El Viejo 2 (EV2), and El Volcán faults), which affected the EVV and EAV. The La Reforma fault, a right-lateral strike-slip fault with a minor normal component, is approximately tangent to the LRC at its southwestern limit (e.g., Garduño-Monroy et al. 1993; Macias-Vásquez and Jiménez-Salgado 2012). The EAC is bounded to the west and the east by El Aguajito and El Alamo faults, respectively. N–S and NE–SW trending faults traverse this eruptive center (i.e., El Cimarrón Fault). N–S to NE–SW minor fault systems are observed to the west and southwest of the TVVC (Fig. 1). Northwest of LVV, the La Virgen fault, seems to be a continuation of the El Campamento fault to the southeast.

Mexico's Federal Commission of Electricity (CFE) has mapped fault systems to aid geothermal exploitation in the TVVC and neighbouring EAC (e.g., López-Hernández et al. 1993; Gomez and Rocha 2009; Benton et al. 2011). Hydrothermal manifestations have been located in some parts of the main fracture systems [e.g., the EV1 and El Azufre faults, Prol-Ledesma et al. 2016], but also in the Las Viboras (LVF) and EV1 faults (Portugal et al. 2000). From electromagnetic studies (Romo-Jones et al. 2018), a hydrothermal

potential zone was inferred, which is located between the TVVC and the EAC (Fig. 1), whose depths reach between 1.5 and 12 km. Furthermore, in the TVVC area has been considered an exploitation reservoir of 6 km^2 and a thickness of 0.3 km (Tello-López et al. 2015), with a thermal state characterized by temperatures of 300 °C (Portugal et al. 2000). Romo-Jones et al. (2000) and Wong et al. (2001) suggested that the TVVC area presents fractured rocks and fluids with temperatures higher than 240 °C at depths between 1.5 and 2.5 km. Since the TVVC is located in the southern part of BC, a homogeneous belt with a Curie isotherm could

reach between 15 and 21 km in depth (Campos-Enríquez et al. 2019).

Data analysis and methods

From 2009 to 2013, the CFE operated a network of twenty seismic stations in and around the TVVC (Lermo et al. 2014) spanning approximately an area of 15 times 15 km. Of this network, only ten sites with seismic stations were part of a permanent seismic network (Fig. 2), which consisted of Guralp CMG-6TD broadband seismographs with three digital components and a sampling interval of 0.01 s. The number of stations in operation changed during this study period (see Table 1).

A total of 558 seismic waveforms with a clear reconnaissance of the arrivals of the P and S phases were analyzed. Their magnitudes M_d, based on duration, vary from 1.0 to 3.0 with depths from 1.0 to 10.0 km, which were calculated with a minimum of four stations, using the SEISAN package (Ottemöller et al. 2013) and considering a location error (RMS) less than 0.5 km. Most of the seismic events were mainly concentrated in the central part of the TVVC, in the area limited to the west by La Virgen Fault and to the east by La Reforma Fault, and concentrated in the area of the EPO, EV1, and EV2 faults (Fig. 2). Secondary seismic groups can also be observed to the north of the EVV, near the El Cimarron Fault, and also to the south and southeast of LVV, near stations TV21, TV22, and TV23.

To estimate the shear-wave splitting parameters (φ and δt), the seismic waveforms were selected and processed following the methodology of Ando et al. (1980) and Bowman and Ando (1987). The developed hybrid code is based on the cross-correlation method, whose details are given in Chacón-Hernández, et al. (2021b). In short, for each event, the horizontal waveform components (N–S and E–W) were rotated in the horizontal plane, finding the maximum of the cross-correlation function within an ideal time window and
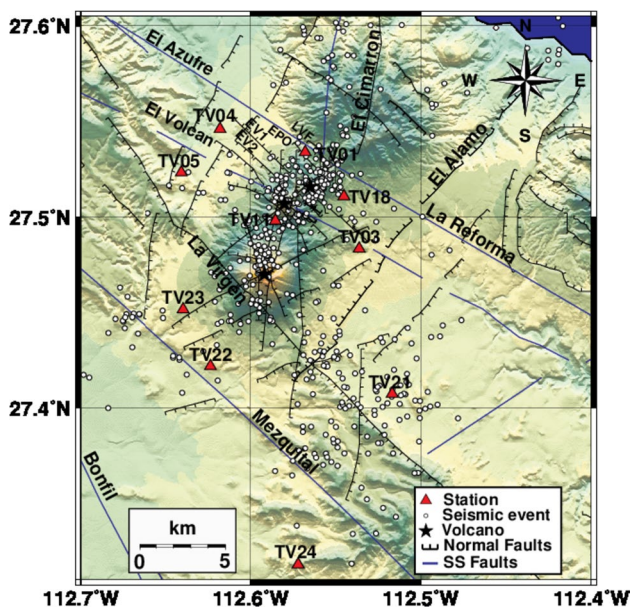

Fig. 2 Main local and regional faults, seismic stations, and seismic events recorded from 2009 to 2013. The northernmost black star represents EVV; the black star in the central sector represents EAV, while the southernmost black star represents LVV. EPO: El Partido fault; LVF: Las Viboras Fault; EV1: El Viejo 1 Fault; EV2: El Viejo 2 Fault; SS Fault: Strike-Slip Fault

Table 1 Location of seismic stations

Station	Latitude	Longitude	Height	2009	2010	2011	2012	2013
TV01	27.53388	−112.56777	710 m	BB	BB	BB	BB	BB
TV03	27.48333	−112.53611	460 m	AC	BB	BB	BB	BB
TV04	27.54611	−112.61777	360 m	BB	BB	BB	BB	BB
TV05	27.52333	−112.64055	400 m	BB	BB	BB	BB	BB
TV11	27.49805	−112.58527	968 m	BB	BB	BB	BB	BB
TV18	27.51083	−112.545	600 m	BB	BB	BB	BB	BB
TV21	27.4075	−112.51666	366 m	–	–	–	BB	BB
TV22	27.42194	−112.62333	403 m	–	BB	BB	BB	BB
TV23	27.4515	−112.63944	525 m	–	–	BB	BB	BB
TV24	27.31805	−112.57194	373 m	–	–	–	BB	BB

AC Accelerometer, *BB* Broadband station (Lermo et al. 2014)

considering an azimuth range from $-180°$ to $180°$, all of which enable to split into two orthogonally polarized components the S-wavefield. The angle with the maximum cross-correlation function provides the fast polarization direction, while the difference in time between both phases (S_1 and S_2) represents the delay. Seismic signals with an incident angle higher than 45° (outside the shear-wave window) were discarded to avoid distortion in the incoming wave, ensuring that the particle motion is not contaminated by S-to P-wave conversions, as recommended by Evans (1984) and Booth and Crampin (1985). To better differentiate S_1 and S_2, the waveforms have been analyzed and subjected to Butterworth filters, especially band-pass filters with frequency range between 0.1, 5, 10, 15, and 20 Hz. However, in some cases, low-pass filters with frequency limits of 15 and 20 Hz were also employed. To calculate the percentage of anisotropy (A), the average anisotropy along the raypath is approximated by the expression:

$$A = (V_s \times \delta t \times 100)/r, \tag{1}$$

where V_s is the shear-wave velocity, δt is the delay time parameter, and r is the source–receiver distance (e.g., Maher and Kendall 2018). The V_s values were approximated considering the arrival time difference between the P and S

phases of each seismic event analyzed and the local ratio $V_p/V_s = 1.70$ (Lermo-Samaniego et al. 2014) used in the study area.

Results

Delay time and the anisotropy strength

Mean delay times (MDT) with their respective errors (Er) (95% confidence level) were obtained from 770 δt values for each station and for each year of the studied period (see Table 2). Stations TV01, TV03, TV04, TV11, TV18, and TV21 presented the highest MDT values, whose variations between years were notable in some cases. For instance, at station TV01, values of MDT range from 0.0531 s during 2010 to 0.0367 s during 2011; while at station TV03, values of MDT vary from 0.0356 s during 2011 to 0.0519 s during 2013 (see Table 2 and Fig. 3). Some of these MDT values were calculated with few data (e.g., for station TV04 during 2010 and 2011; for station TV18 during 2010 and 2013, see Table 2 and Fig. 3). On the other hand, the lowest MDT values can be observed at some stations for particular years (e.g., at station TV05 during 2010 and 2012; at station TV24 during 2012 and 2013, Table 2 and Fig. 3). The associated

Table 2 Mean delay time (MDT), the error as 95% confidence level (Er), and the number of used data (UD) for all seismic stations from 2010 to 2013

St	2010			2011			2012			2013		
	MDT (sec)	Er	UD	MDT (sec)	Er	UD	MDT (sec)	Er	UD	MDT (sec)	Er	UD
TV01	0.0531	0.0108	29	0.0367	0.0073	44	0.0434	0.0061	77	0.0417	0.0116	22
TV03	0.0373	0.0223	8	0.0356	0.0067	30	0.0435	0.008	50	0.0519	0.0225	12
TV04	0.0502	0.0196	13	0.0567	0.0205	7	0.0466	0.0097	45	0.0514	0.0193	5
TV05	0.0094	0.0	1	0.0315	0.0061	3	0.0332	0.0102	21	–	–	–
TV11	0.0492	0.0165	21	0.0542	0.0098	43	0.0408	0.0058	73	0.0471	0.0095	34
TV18	0.0483	0.0299	9	0.0442	0.0097	35	0.0384	0.0071	49	0.0538	0.0192	11
TV21	–	–	SNI	–	–	SNI	0.0364	0.0143	11	0.0587	0.0145	7
TV22	–	–	–	0.0276	0.0137	11	0.0314	0.011	23	–	–	–
TV23	–	–	SNI	0.0418	0.019	9	0.0384	0.0081	43	0.0365	0.0159	15
TV24	–	–	SNI	–	–	SNI	0.0159	0.0066	8	0.0283	0.0	1

SNI Station not installed. *St* Station

Fig. 3 MDT values and their respective error bars (95% confidence level) for each seismic station during each year
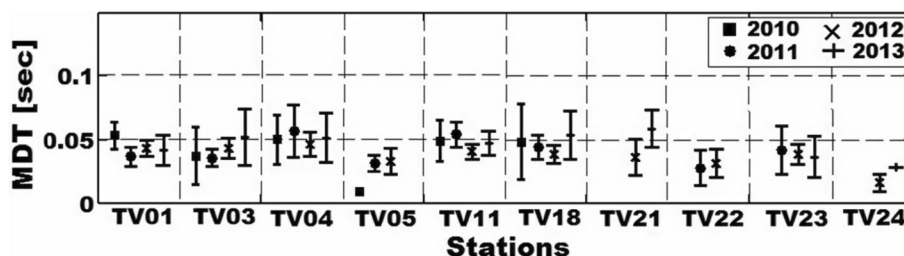
errors (95% confidence intervals) do not show significant changes, but the TV03 and TV18 stations, both during the years 2010 and 2013, show large error bars compared to the other years and stations (Table 2 and Fig. 3).

The mean anisotropy percentage (MAP) was obtained with its respective error (95% confidence level) for each seismic station and each year (Table 3 and Fig. 4). The highest A values are mainly observed in station TV01 during 2010 and 2012; in station TV04 during 2011 and 2013; in station TV11 during 2011; and in station TV18 during the years 2010 and 2013, generally exceeding 2.0%. Noteworthy is a marked increase from 2012 to 2013 in all stations, except for the TV01 and TV11 stations, which show a decrease (Fig. 4). Most of the MAP values are between 0.54 and 2.53%, whose associated errors (95% confidence interval) approximately overlap in some years (e.g., station TV03 during 2010 and 2013; station TV04 during 2010, 2011, and 2013; station TV05 during 2011; station TV11 during 2010; station TV18 during 2010 and 2013; station TV22 during 2011; station TV23 during 2011 and 2013), which indicate notable variations in anisotropy measurements (see Fig. 4). The largest variation in the error ranges is observed in stations TV04, TV18, and TV21, which also present high MAP values, while lowest errors are mainly observed in stations TV01 and TV11 (see Table 3 and Fig. 4).

All data used to calculate the MDT and MAP values at each seismic station (Tables 2 and 3 and Figs. 3 and 4) are collected in Fig. 5, showing the distribution of the δt and A values with respect to depth. Their respective MDT and MAP values are indicated. The highest δt and A values (> 0.1 s and 5.5%) are mainly located in a narrower depth range, approximately for seismic events from 3.0 to 7.0 km for the δt (Fig. 5a) and A values (Fig. 5b). Lower values (< 0.05 s and 2.0%) can be associated with seismic events of all depths (from 3.0 to 10.0 km), but values for events deeper than 9.0 km do not exceed 0.1 s and 3.0%, respectively. Their respective mean values MDT and MAP were calculated along with their respective errors at a 95% confidence level.

Spatial distribution of the highest anisotropy percentage

Figure 6 shows the hypocentral distribution of 60 seismic events recorded at all stations and analyzed to calculate the A value. The range represented a delay time of 0.075 s for the A value of 4.02% to a delay time of 0.104 s for 10.3%. A values above 4.02% are important to delimit areas with high fracturing levels (e.g., Crampin 1994). The highest A values are found in the area of the volcanic complex, especially between EVV and EAV, near the El Azufre, El Volcán, EPO, EV1, and EV2 faults and other unnamed faults (see Fig. 6). Respective depths of the seismic events analyzed range between 3.0 and 6.5 km. Other seismic events for which significant A values have been obtained are located

Table 3 Mean anisotropy percent (MAP), the error as 95% confidence level (Er), and the number of used data (UD) for all seismic stations from 2010 to 2013. SNI: Station not installed. St: Station

St	2010			2011			2012			2013		
	MAP (%)	Er	UD	MAP (%)	Er	UD	MAP (%)	Er	UD	MAP (%)	Er	UD
TV01	2.25	0.5	29	1.80	0.54	44	2.22	0.37	77	1.89	0.61	22
TV03	1.49	1.13	8	1.39	0.31	30	1.79	0.33	50	2.10	0.92	12
TV04	1.89	0.83	13	2.14	1.48	7	1.65	0.52	45	2.17	1.24	5
TV05	0.54	–	1	1.71	0.95	3	1.33	0.46	21	–	–	–
TV11	1.97	0.78	21	2.53	0.55	43	1.58	0.24	73	1.89	0.38	34
TV18	2.53	1.98	9	1.99	0.57	35	1.78	0.35	49	2.50	0.89	11
TV21	–	–	SIN	–	–	SNI	1.81	0.83	11	1.99	1.16	7
TV22	–	–	–	1.28	0.82	11	1.09	0.43	23	–	–	–
TV23	–	–	SNI	1.90	0.95	9	1.41	0.3	43	1.69	0.81	15
TV24	–	–	SNI	–	–	SNI	0.63	0.32	8	1.18	–	1

Fig. 4 MAP values and their respective error bars (95% confidence level) for each station during each year
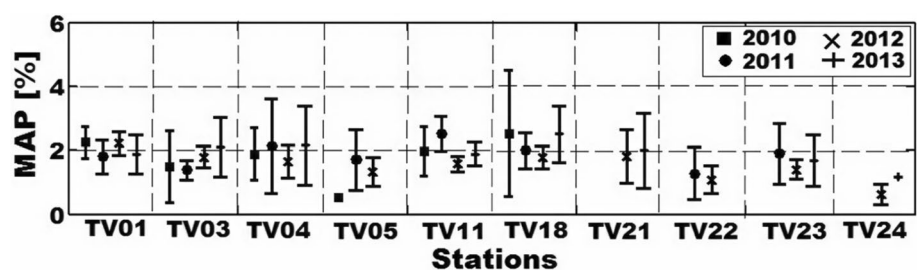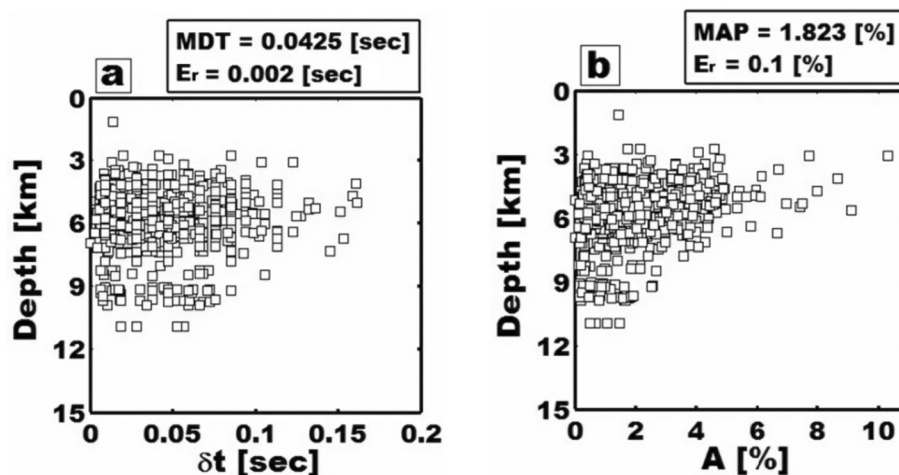
Fig. 5 Shear-wave splitting delays vs. depth **a** and percent of anisotropy vs. depth **b**. The mean delay time, MDT, the mean anisotropy percentage, MAP, and their respective errors Er (95% confidence level) are shown on top of each plot

to the south and southwest of LVV, close to the La Virgen and Mezquital faults and to the TV21, TV22, and TV23 stations, but also near the El Volcán fault and the TV05 station, whose depths mainly range between 6.0 and 7.0 km.

Analysis of the main pathways with high fracturing

In particular and to simplify the estimation of the anisotropy percentage, the raypath lengths used to normalize δt were approximated by the lengths of straight lines joining the hypocentral depth of each event and the recording station. Figure 7a shows all pathways (straight lines) joining the seismic sources and stations. These pathways were differentiated based on three criteria: (1) Only those anisotropic pathways with anisotropy percentages greater than 4.0% are considered; (2) ranges from 4.0 to 7.0, 7.1 to 9.0%, and greater than 9.0% are used to differentiate high levels of fracturing; (3) Most of these pathways had angles of incidence less than 45°. Figure 7a and b show in isometric and map views the pathways with an anisotropy percentage above 4.0%, which help to highlight the zones with the highest fracture degrees. These figures include pathways obtained from seismic events from all the years of the studied period. There are no pathways with large fracture levels arriving to stations TV05 and TV24. In the isometric view, the pathways with the highest percentage of anisotropy (i.e., A ≥ 7.1%) are represented by those straight lines formed by both sequences of dark red squares with black frames and pink squares with light red frames, while those pathways with A values between 4.0 and 7.1% are represented by sequences of blue squares (see symbology). All these anisotropic pathways were derived from seismic events that have their origins at depths between 3.0 and 7.0 km, but mostly at depths between 4.0 and 6.0 km (Fig. 7b).

These anisotropic pathways were projected onto a horizontal plane (Fig. 7c). A high fracturing zone can be noted to the east and northeast of EVV (Fig. 7c), where the La

Reforma and El Azufre faults (numbers 1 and 10 in Fig. 7c) interact with the El Cimarron (number 9 in Fig. 7c) and other unnamed N–S to NE–SW faults (i.e., faults not marked with numbers in Fig. 7c). High fracturing is also present around EAV, where El Volcán Fault (number 2 in Fig. 7c) and minor NW–SE faults (possible southward extensions of EV1, EV2, and EPO faults (numbers 5, 6, and 7 in Fig. 7c), intersect unnamed N–S to NE–SW faults. Another zone with a high level of fracturing is also indicated along the EV2 and EPO faults (numbers 6 and 7 in Fig. 7c). In general, high fracturing is inferred to be beneath the EVV and EAV (Fig. 7c). These pathways mainly cross the substratum of La Reforma, El Volcán, EV1, EV2, and EPO faults, as well as to the EVV, LVV, and EAV structures. Other pathways can also be observed near the La Virgen-El Campamento and El Mezquital faults, arriving at stations TV21, TV22, and TV23 (Fig. 7c). Figure 7d represents an approximately NW–SE vertical section through stations TV01, TV04, and TV18 following the La Reforma and El Azufre faults, highlighting pathways with high percentage of anisotropy from seismic events at depths of 3.0 to 6.5 km. Figure 7e represents an NE–SW vertical section through stations TV01 and TV18, highlighting pathways with high percentage of anisotropy from seismic events at depths of 3.5 to 6.5 km.

In Fig. 8a, the anisotropic pathways with the highest fracture densities are projected onto a geological profile, where most of the anisotropic trajectories converge toward the EVV, an intermediate concentration beneath the EAV, with a lower concentration around the LVV. The stratigraphic units are described in Table 4 according to Avellán et al. (2018). The origins of the pathways begin from seismic events inside the Peninsular Ranges Batholith unit (PRB) (approximately from 7.0 to 4.0 km) and cross other more superficial geological units (i.e., in the Santa Lucia-San Francisco (SL-SF), Esperanza Basalt (EB), Aguajito ignimbrite (Ag), Lower Viejo dacitic lava dome (LVdld),

Fig. 6 Hypocentral distribution of the seismic events analyzed with a percentage of anisotropy higher than 4.02%. (Top) The size of the circles represents the A values, where the largest corresponds to the maximum (10.03%) and the smallest to the minimum (4.02%). The depths of these earthquakes are indicated by the grayscale. The northernmost black star represents EVV; the black star in the central sector represents EAV, while the southernmost black star represents LVV. (Bottom) Zoom of the area delimited in the Fig. 6a by the black rectangle, yellow triangles indicate producing wells, while green triangles indicate injection wells
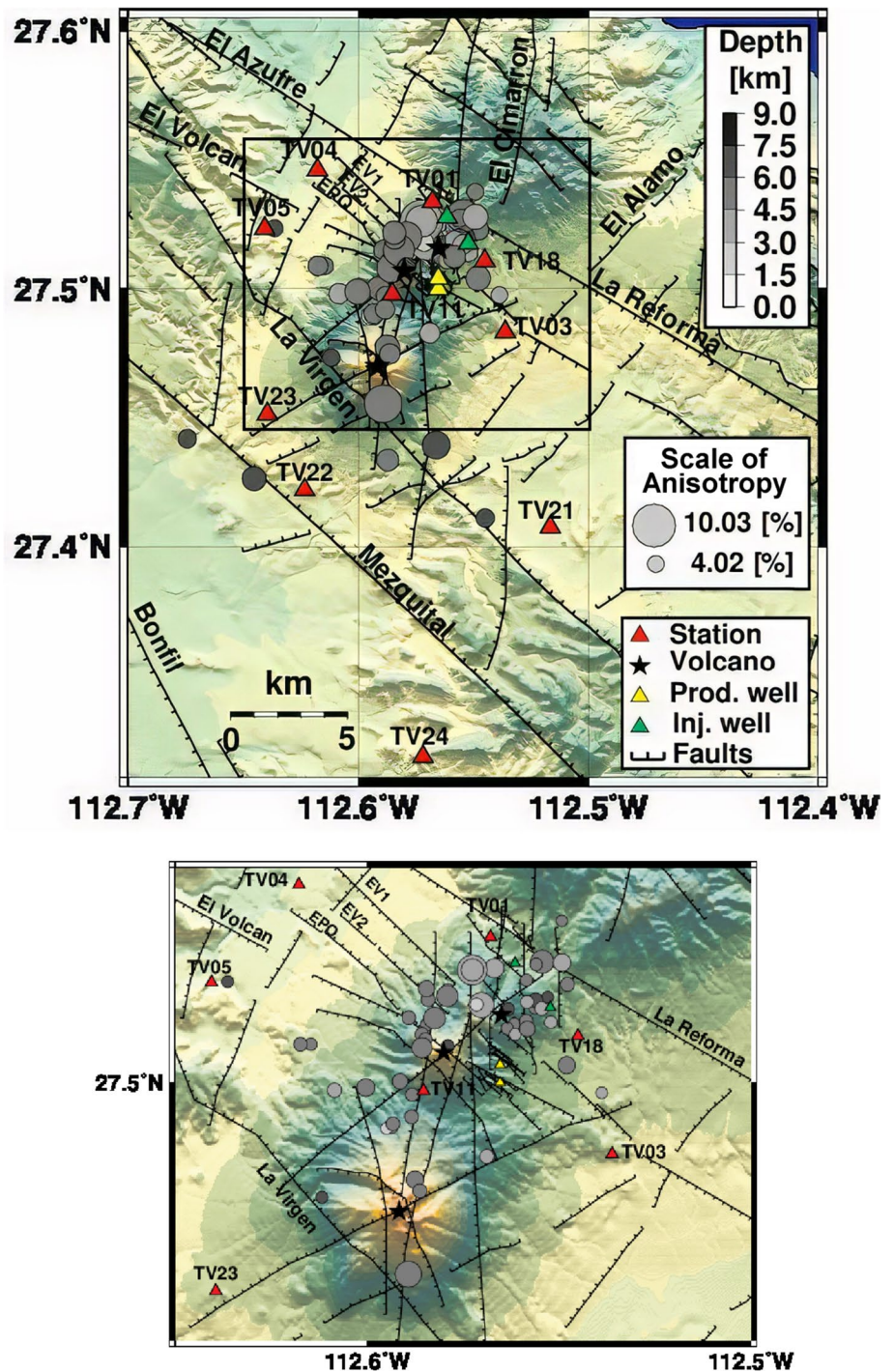
Puerta dacitic lava dome (Pdld), and Upper Viejo dacitic lava dome (UVdld) units), as well as different faults. Figure 8b shows the projected anisotropic pathways onto a plane (map view) at sea level (i.e., 0 km), which approximately coincides with the top of SL-SF unit. In Fig. 8c, the intersection of the anisotropic pathways is shown onto a section of approximately 1.0 km deep below sea level that approximately coincides with the top of the PRB unit. Meanwhile, Fig. 8d, e, and f show the anisotropic pathways projected onto planes at depths of 2.0, 3.0, and 4.0 km, reaching deeper parts of the PRB unit. These projected anisotropic pathways show how some areas with high fracturing cover these geological units.
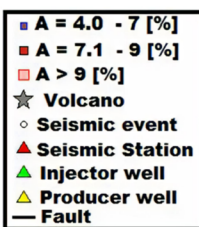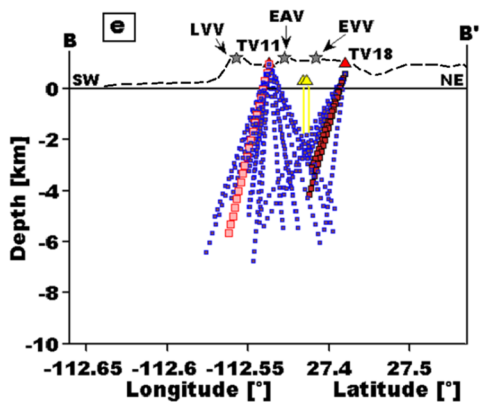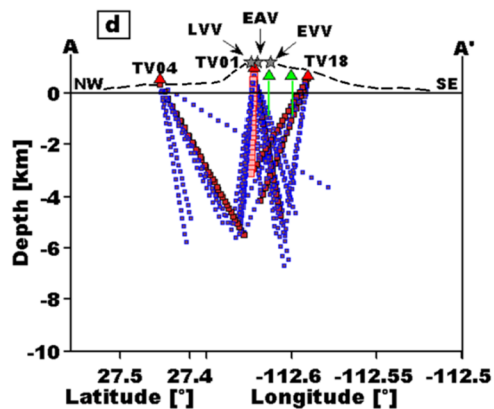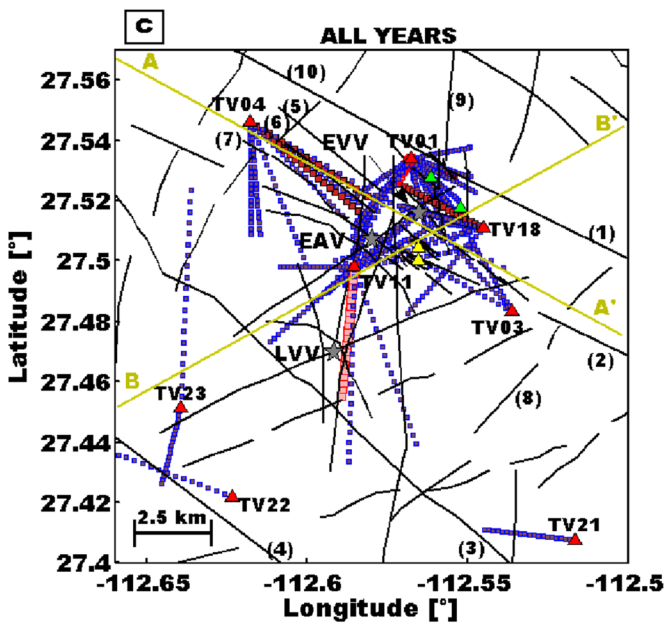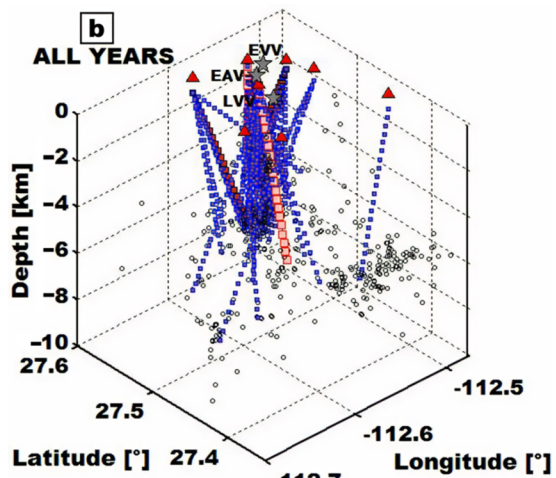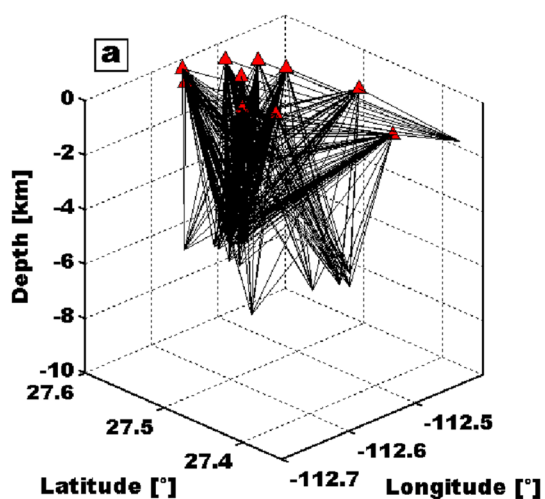
◄**Fig. 7** The set of all the anisotropic pathways approximated by straight lines that were analyzed **a**. Pathways with anisotropic values larger than 4.0 are displayed in an isometric view **b** and map view **c**. The displayed pathways are associated with A values in three ranges (4.0–7.0, 7.1–9.0, and > 9.0%, see symbology). Yellow lines in **c** indicate the locations of the NW–SE vertical section that respectively cut through stations TV01, TV04, and TV18 **d** and through stations TV01 and TV18 **e** with anisotropic pathways projected on these planes; the respective surface topography is shown in dashed black lines. The names of the faults are: (1) La Reforma, (2) El Volcán, (3) La Virgen-El Campamento, (4) El Mezquital, (5) EV1, (6) EV2, (7) EPO, (8) El Alamo, (9) El Cimarron, and (10) El Azufre. Unnamed N–S to NE–SW faults are not marked with numbers in Fig. 7b

Analysis of delay times vs. seismic frequencies and anisotropy vs. shear-wave velocities

Two examples of seismic events with similar hypocentral parameters and recorded at station TV11 (the event 2010-05-13-1938-31S.CFE of Fig. 9a: Latitude: 27.5201°, Longitude: −112.5792°, Depth: 5.2 km; the event 2010-05-13-1958-26S.CFE of Fig. 9b: Latitude: 27.5209°, Longitude: −112.5792°, Depth: 5.1 km) illustrate variations on the shear-wave splitting delays and spectral frequency contents. Both seismic events were subjected to band-pass filters using ranges from 5 to 15 Hz, respectively, to obtain the splitting times, where their fast S_1 and slow S_2 shear waveforms as well as their picked onsets are shown. In the first event (Fig. 9a), the δt value obtained was 0.056 s, with a range of dominant frequencies from 0 to 5.95 Hz; while for the second event (Fig. 9b), the δt value obtained was 0.0094 s, with a range approximately from 0 to 9.0 Hz. In this example, the delay time is shorter when the frequency content is higher and slightly more extended (Fig. 9b), but larger delays when lower frequencies are dominant (Fig. 9a), although this plot shows a second important peak around 5 Hz. Both dominant frequencies were obtained for the fast S-wave forms without filtering to avoid losses and attenuations of the original frequencies.

Figure 10 plots the relationships between values of δt vs. the main seismic frequencies f_{max} (Fig. 10a), which were obtained from the dominant peaks in the seismic frequency spectra from the fast S-waveforms. Likewise, the percentage of anisotropy A vs. shear-wave velocities V_s (Fig. 10b), and f_{max} vs. V_s values (Fig. 10c) of 77 seismic waveforms recorded during 2010 at stations TV01, TV03, TV04, TV11, and TV18 (the closest stations to the geothermal site) is plotted, where the depths of the analyzed seismic events varied mainly from 3.5 to 7.0 km. To avoid filtering, only this year is assessed because most of the fast seismic waveforms presented less noise (i.e., a signal-to-noise ratio greater than 5.0) in contrast to the data from the rest of the years with greater variation. This allowed, in a more exemplified way, to analyze f_{max} along with the behavior of the δt, V_s, and A parameters of the used data. Nonetheless, in the analysis of

the highest anisotropic pathways, information from all years was considered.

Trying to link some effects and phenomena, values of δt, f_{max}, V_s, and A are classified and analyzed according to their behaviors and from information from previous studies. Intermediate and high δt values (above 0.03 s) associated with lower f_{max} values (e.g., from around 0.01 to 1.0 Hz) were grouped in the dashed square GA1 (see Fig. 10a), considering possible effects related to fracture systems with lower fluid content (e.g., van Der Kolk et al. 2001; Liu et al. 2001; Liu et al. 2003; Kozlov 2004). Intermediate and high δt values (above 0.03 s), associated with higher f_{max} values (e.g., above 1.0 Hz), were grouped in the dashed square GA2, considering possible effects of fracture systems with higher fluid content effects (e.g., Chesnokov et al. 2001; Liu et al. 2001; Kozlov 2007). Some data from stations TV01, TV03, TV04, TV11, and TV18 showed lower δt values (from 0.01 to 0.02 s) for different f_{max} values (between 0.5 and 2.0 Hz), which were grouped in the dashed square GA3 (see Fig. 10a). Added to this, data from stations TV04, TV11, and TV18 with lower V_s (e.g., between 1.0 and 2.5 km/s) and A values (e.g., between 0.01 and 2.0%) were also grouped in the dashed square GB1 (see Fig. 10b), this was done considering the possible existence of sealed fractures and effects of magmatic bodies (e.g., Vanorio et al. 2005; Latter 1981). Increasing trends between the A and V_s values are mostly observable for stations TV01, TV11, and TV18 between 0.01 and 5.55%, for A values and between 1.0 and 4.0 km/s for V_s values, but less clear at stations TV03 and TV04 (Fig. 10b).

Figure 10c shows the relationship between the f_{max} and V_s values as a complement of Figs. 10a and b, where most of the data of stations TV01, TV03, and TV18 presented V_s values between 2.5 and 3.0 km/s for f_{max} values less than 1.0 Hz, while most of the data of the TV04 station presented V_s values above 3.2 km/s for f_{max} values less than 1.0 Hz. Two cases can be considered for the data of the TV11 station; in the first, the V_s values ranged between 2.2 and 3.6 km/s for f_{max} values above 1.0 Hz, while for the second case, the V_s values ranged between 1.0 and 2.5 km/s for f_{max} values less than 1.0 Hz. Particular cases are observed for data from stations TV01, TV04, and TV11, with a low range of V_s and f_{max} values (e.g., from 1.0 to 2.5 km/s; from 0.5 to 1.0 Hz, respectively), which were grouped in the dashed square GC1. This grouping is supporting the possible existence of sealed fractures and magmatic body effects. Stations TV11 and TV18 presented the highest f_{max} values (between 1.5 and 2.0 Hz) for V_s values between 2.2 and 3.0 km/s, which are grouped in the dashed square GC2, this is also supporting the presence of fracture systems with higher fluid content. Stations TV01 and TV04, together with other fewer data of other stations, presented the highest V_s values (from 3.0 to
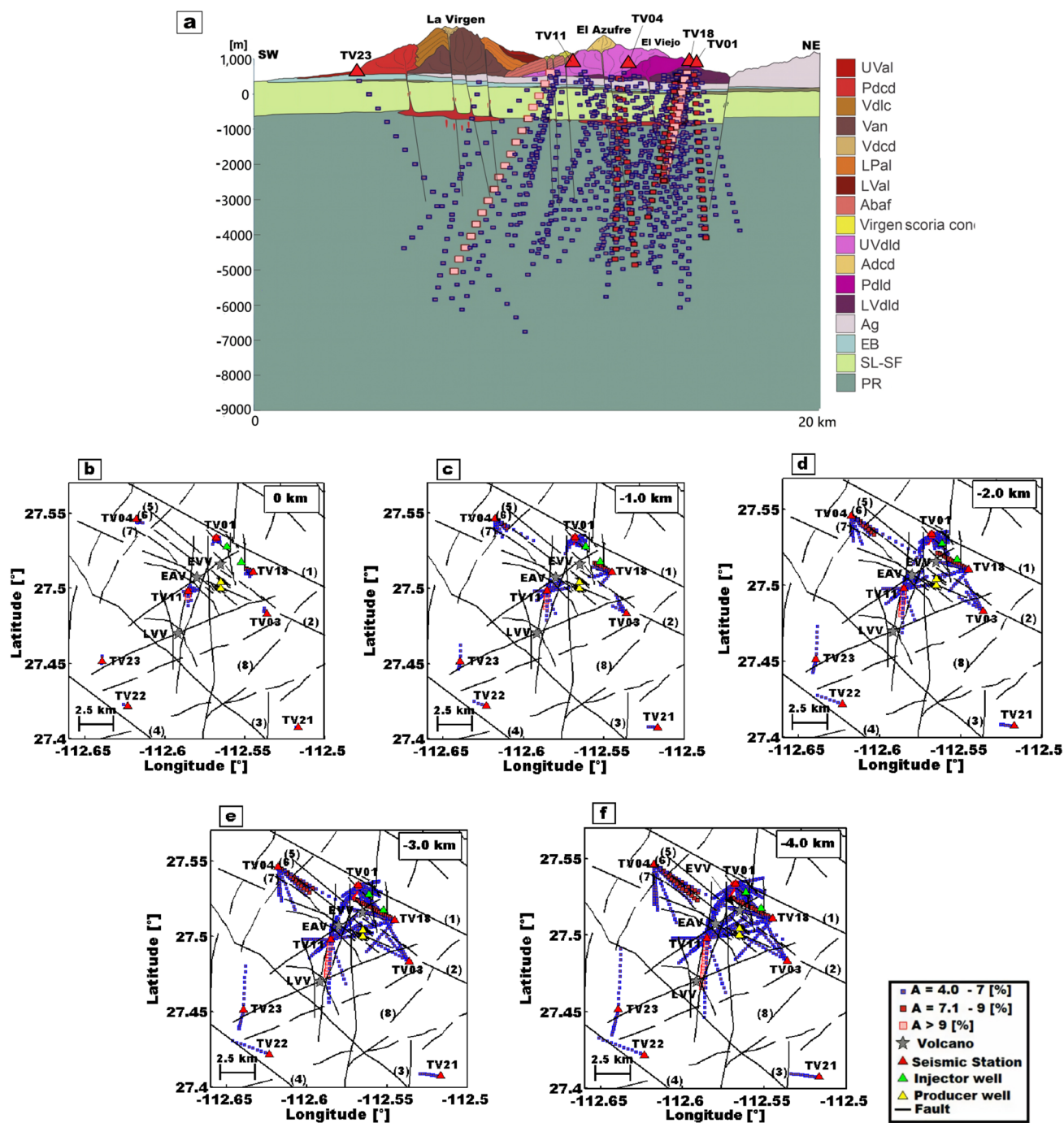
Fig. 8 a Anisotropic pathways recorded in different stations are projected on an approximately NE–SW profile that crosses the volcanoes of the TVVC after Avellán et al. (2018). **b** Intersections of anisotropic pathways onto planes at sea level (i.e., 0 m in Fig. 7a), **c** at depths of approximately −1.0 km (i.e., −1000 m in Fig. 7a) **d** −2.0 km, **e** −3.0 km, and **f** −4.0 km

4.0 km/s) for lower f_{max} values (between 0.5 and 1.0 Hz), which were grouped in the dashed square GC3 supporting the existence of fracture systems with lower fluid content effects. The data between GC1 and GC3 squares presented a range of V_s values mainly between 2.5 and 3.0 km/s, which do not exceed 1.0 Hz. Some data of the GA1 and

GA2 groups present V_s values above 2.5 km/s (covering part of the GC1 and GC3 groups) with A values above 2.5 and up to 8.6%. In the GA3 group, lower A values (less than 1.0%) with a specific range of V_s values (between 2.0 and 3.8 km/s) could be considered to minor fracture systems with lower effects of fluid content or sealed fractures.

Table 4 Description and ages of geological units shown on the profile map in Fig. 8a (after Avellán et al. (2018)

| Uval	Upper Virgen andesitic lava	22 ± 2.5–25.5 ± 4.4 ka
Vdcd	Virgen dacitic central dome	$51 + 8.7/-8$ ka
Pdcd	Pinto dacitic coulee dome	$61 + 7/-6.7$ ka
Lval	Lower Virgen andesitic lava	$89.8 + 9.6/-8.8$ ka
Vdlc	Virgen dacitic lava cone	$102 + 30/-23.8$ ka
Lpal	Lower Pintos andesitic lava	$110.6 + 43/-30.9$ ka
Van	Virgen andesitic neck	–
Vsc (Virgen scoria cone)	Virgen scoria cones	–
Adcd	Azufre dacitic central dome	$153.9 + 32/-25$ ka
Abaf	Azufre block and ash flow	$146 + 27.8/-22$ ka
UVdld	Upper Viejo dacitic lava dome	254 ± 24 ka
Pdld	Puerta dacitic lava dome	–
Lvdld	Lower Viejo dacitic lava dome	–
Ag	Aguajito ignimbrite	1.17 Ma
EB	Esperanza basalt	7.64 ± 1.16 Ma
SL-SF	Santa Lucia-San Francisco	21.6 Ma
PRB	Peninsular Ranges Batholith	99.1 ± 0.8 Ma
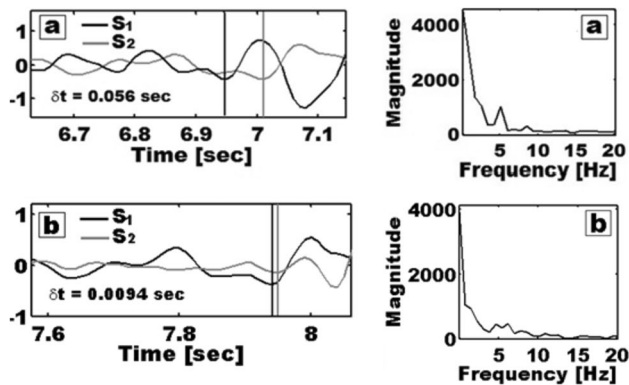
Fig. 9 Fast S_1 and slow S_2 shear waveforms with their respective picked onsets of a pair of events with similar hypocentral parameters (event of **a**: 27.5201°, − 112.5792°, 5.2 km depth; event of **b**: 27.5209°, − 112.5792°, 5.1 km depth). The picked onsets of the shear waveforms are indicated. Seismic frequency spectra were calculated from the fast S-waveforms without filtering, which are also displayed

The data between the GC1, GC2, and GC3 groups would not clearly evidence one phenomenon as mentioned above (Fig. 10c), but rather a combination of the presence of several phenomena. Station TV01 presents a greater amount of data, while stations TV03 and TV18 comprise a smaller amount of data.

Figure 11 shows the epicenter locations of each seismic data group analyzed in Fig. 10. The seismic events of the GA1 group (events in brown color and recorded at each station as shown in the symbology, Fig. 11a), originated mainly from the north and south of EVV and EAV and

near the TV11 station (Fig. 11a), present a depth range from 3.6 to 6.8 km, but the seismic signals recorded at station TV03 have hypocenters located in a narrower depth range (i.e., more concentrated around a depth range, from 4.6 to 5.1 km, Table 5). The seismic events considered for the GA2 group (events in blue color, Fig. 11b) are originated from several locations along the EAV and EVV, whose depths vary from 3.5 to 6.0 km. The origin of seismic events in some stations presented narrower depth ranges, going from 5.5 to 6.0 km at station TV03, 5.5 km at station TV04, and from 5.0 to 5.2 km at station TV11 (Table 5). The area comprising seismic events of the GA3 group (events in cyan color, Fig. 11c) is broader and includes the locations of groups GA1 and GA2. The seismic events of these groups are mainly located around EAV and EVV and to the south of EAV, with depths range from 4.1 to 6.0 km, presenting the TV04 and TV18 stations with narrower depth ranges (from 5.4 to 6.0 km, and from 4.9 to 5.3 km, respectively, Table 5). The origin of seismic events in group GB1 (events in light pink color, Fig. 11d) is mainly located around EVV and EAV and near stations TV01, TV11, and TV18, whose depths range from 4.0 to 7.0 km, presenting narrower depth ranges the TV04 station (from 5.2 to 5.5 km, Table 5). The origin of seismic events analyzed in the GC1 group (events in brown color, Fig. 11e) is mainly located to the west of EVV and EAV, with depths from 4.4 to 6.0 km, presenting the TV01 and TV04 stations narrower depth ranges (from 5.1 to 5.7 km, and from 5.0 to 5.7 km respectively, Table 5). Some of their locations coincide with that of group GA1. The origin of seismic events analyzed in the GC2 group (events in blue color, Fig. 11f) is located around the volcanic complex, with a depth range from 5.0 to 6.0 km, presenting all the stations narrower depth ranges (see Table 5). The origin of seismic events analyzed in the GC3 group (events in cyan color, Fig. 11g) is located around the EAV and EVV structures and mainly located in north and south of EAV and EVV and near the TV11 and TV18 stations, with a depths range from 4.4 to 6.0 km. Their location correlates with that of the GA3 and GB1 groups.

Figure 12a and b display the relationships between δt vs. f_{max} and A vs. V_s values of 16 seismic waveforms recorded during 2010 at stations TV01, TV03, TV04, TV11, and TV18. This was done considering a hypocentral seismic depth between 4.0 and 5.0 km. Meanwhile, Fig. 12c and d presents these relationships for 49 seismic waveforms considering a hypocentral seismic depth between 5.0 and 6.0 km. The plots seem to show differences, with f_{max} values reaching a maximum of 1.0 Hz for those seismic events with a depth range between 4.0 and 5.0 km (Fig. 12a). The seismic events with a depth range from 5.0 to 6.0 km can reach up to 2.0 Hz, although most of the data present f_{max} values around 1.0 Hz (Fig. 12c).

Fig. 10 **a** Delay times vs. f_{max}, **b** percentage of anisotropy vs. shear-wave velocities, and **c** f_{max} vs. shear-wave velocities obtained from 77 seismic events recorded at stations TV01, TV03, TV04, TV011, and TV18 during 2010
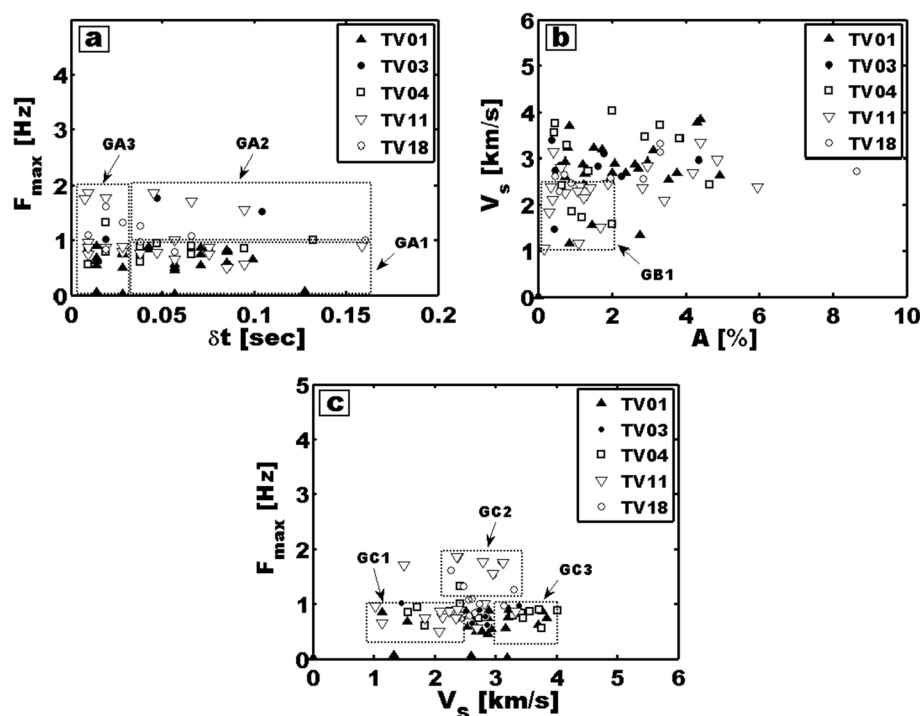
Likewise, a narrow range of V_s values (between 2.0 and 3.8 km/s) is observed for those seismic events with a depth range between 4.0 and 5.0 km (Fig. 12b), spanning a wide range of A values from 0.02 to 6.0%. Meanwhile, for those seismic events with a depth range between 5.0 and 6.0 km, a range of V_s values from 2.0 to 3.5 km/s is observed, with some V_s values less than 2.0 and above 3.5 km/s. The A values span a wide range from 0.02 to 5.0% (Fig. 12d).

Discussion

Fracturing systems with respect to depth

In Fig. 13, are shown the fast polarization directions from seismic events originated at different depth intervals (the hypocenters of the used events are shown in Fig. 15). Only those seismic events that arise in the close neighborhood of each of the stations TV01, TV03, TV11, and TV18 [< 0.035° in latitude and longitude and with angles of incidence less than 45° (Evans 1984; Booth and Crampin 1985)] were considered in this analysis. The main relative fast polarization direction observed at all depths is NW–SE, whose associated mean fast polarizations M vary approximately between − 120° and − 13.2° (obtained with the aid of the CircStat program by Berens 2009). The mean resultant length R, which gives a quantitative estimate of the data variance, falls mainly above 0.3 but lesser than 0.5 at the four analyzed stations, which could represent an intermediate data clustering (e.g., less than 0.3 could represent a bad clustering, Peng

and Ben Zion 2004). The TV01 station presented the highest R values for more depth ranges (i.e., > 0.52 except in the depth range of 6–7 km), whose mean polarizations follow the orientation of the El Volcán fault (e.g., Fig. 2). Some other fast polarization directions have also been observed in these stations for different depth levels (see Fig. 13), which evidenced the existence of fracture systems in other directions. For instance, for those events originating between 3.0 and 4.0 km depth and for stations TV03 and TV18, WNW–ESE and NE–SW polarization directions are also observed (Figs. 13a and b). For seismic events in the depth intervals of 4–5 and 5–6 km, NNE–SSW and NE–SW secondary polarizations are a feature at all four stations except at station TV11 (Fig. 13c). These NNE–SSW and NE–SW polarizations are of lower importance at the 3–4 km depth interval in all stations except at station TV18 (Fig. 13d). For seismic events at deeper levels, the presence of NNE–SSW and NE–SW fast polarizations is also observed, but with low importance (e.g., seismic events recorded at station TV01 with focal depths from 6.0 to 9.0 km; seismic events recorded at station TV03 with depths from 6.0 to 7.0 km; seismic events recorded at station TV11 with depths from 6.0 to 8.0 km; seismic events recorded at station TV18 with depths from 6.0 to 8.0 km, Fig. 13). At station TV01, behaviors between values of ϕ and f_{max} show a large concentration between − 75 and 0° for f_{max} values less than 1.0 Hz, mainly related to the 6–7-km depth interval (Fig. 13a). At station TV03, no particular behavior is observed for each depth interval, except for the 4–5-km interval with higher f_{max} values, which reach between 4.0 and 6.0 Hz for ϕ values
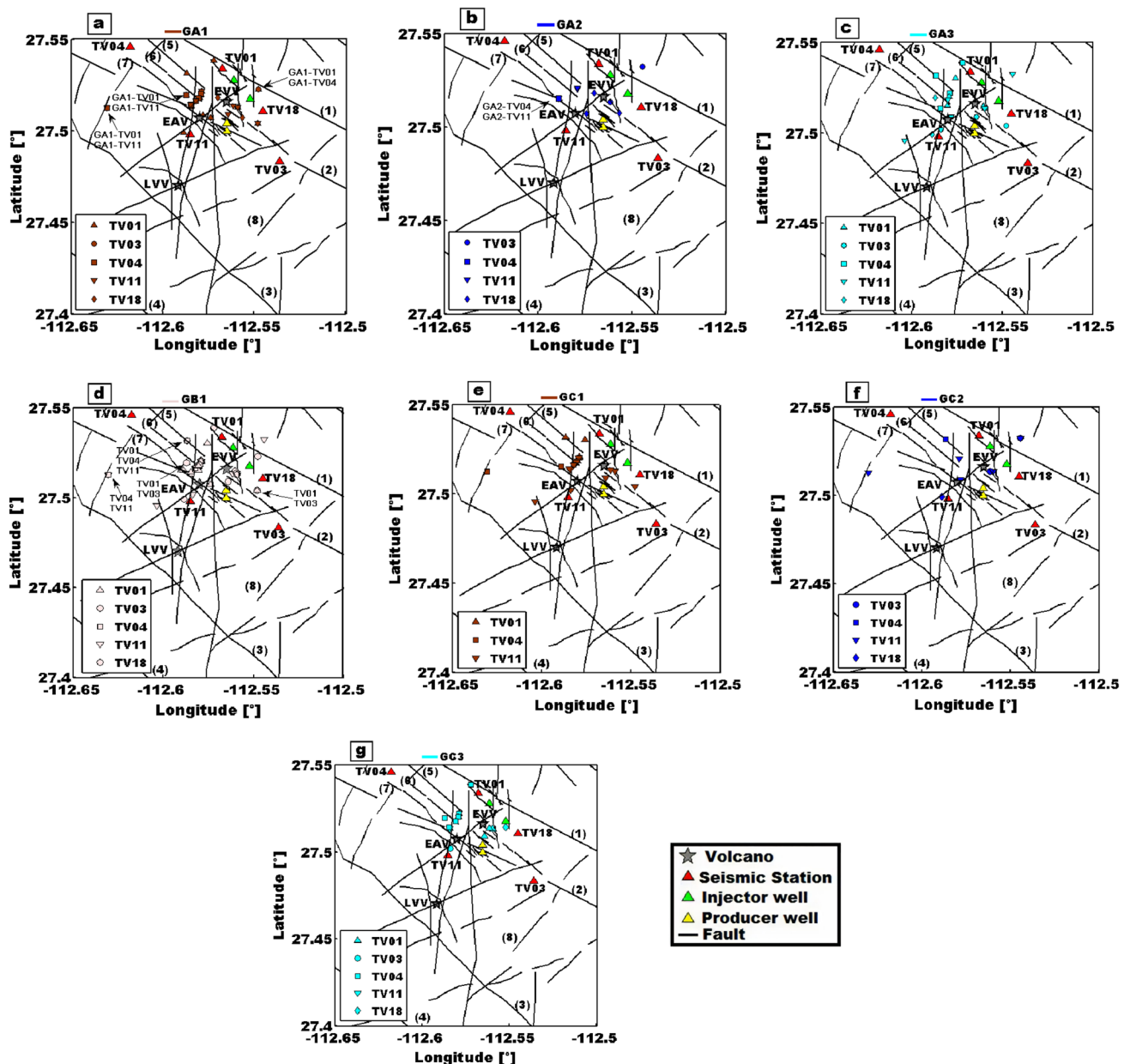
Fig. 11 a Epicenter locations of the seismic events analyzed in the GA1, GA2, and GA3 groups for each station of Fig. 10a, b and c) the GB1 group of Fig. 10d, and the GC1, GC2, and GC3 groups of Figs. 10e, f, and g. Because seismic waveforms from a same analyzed seismic event were recorded at different stations, some epicenters of the different data groups have the same location. They are indicated by black arrows. The symbology of the stations TV01, TV03, TV04, TV11, and TV18 is indicated at the bottom of each map, representing the recording station from the events of each analyzed group

between 0 and −70° (Fig. 13b). At station TV11, most of the φ values fall between −90° and 0° for most of the depth intervals, with values less than 1.0 Hz; nonetheless, for the particular case of the 6–7 km depth interval, the f_{max} values are higher than 1.0 Hz (Fig. 13c). At station TV18, in the 4–5 and 5–6-km intervals, most of the results fall between 10° and -90°, whose f_{max} values are in a range of 0.1 and 2.0 Hz with some particular cases higher than those (Fig. 13d).

Figure 14 shows the relationship between the δt parameter and the hypocentral distance for stations TV01, TV03, TV11, and TV18, considering seismic events less than 0.035° in latitude and longitude, and depths less than 5.0 km. This depth limit is considered only to establish the depth at which the pervasive anisotropy begins. Theoretically, at greater hypocentral distances, higher δt values would be expected. However, in both plots, it is possible to observe for each station both high and low

Table 5 Summary of the different depth ranges of the analyzed seismic events for each station of each group (i.e., GA1, GA2, GA3, GB1, GC1, GC2, and GC3) in Fig. 11

Group	Depth (km)				
	TV01	TV03	TV04	TV11	TV18
GA1	4.6–6.8	4.6–5.1	4.9–5.9	4.4–5.9	3.6–6.0
GA2	–	5.5–6.0	5.5	5.0–5.2	3.5–4.9
GA3	4.1–5.5	4.4–6.0	5.4–6.0	4.4–6.0	4.9–5.3
GB1	4.0–7.0	4.5–5.5	5.2–5.5	5.0–6.0	5.0–6.0
GC1	5.1–5.7	4.3	5.0–5.7	4.4–6.0	–
GC2	–	5.5–6.0	–	5.0–6.0	5.3
GC3	4.4–5.5	6.01	5.0–6.0	5.4	3.4

δt values for given hypocentral distances. In particular, an unusual behavior of high δt values for smaller hypocentral distances could be an indication of a high concentration of fractures at shallower depths. Thereby, in Fig. 14a, an anisotropic and pervasive stratum can be considered for some events recorded in station TV01 to start at a hypocentral distance of 3.5 km for some values observed, for which the highest normalized delay time is $\delta t_n = 31.95$ ms/km, while a mean with a 95% confidence level is $\delta t_n = 10.6 \pm 0.007$ ms/km. Seismic events recorded at station TV03 do not show clear evidence of a pervasive stratum. In Fig. 14b, this unusual high fracturing is also possible to observe for some events recorded in station TV18 from hypocentral distances of 4.5 km,

whose highest normalized delay time is $\delta t_n = 26.17$ ms/km, while a mean with a 95% confidence level is $\delta t_n = 10.77 \pm 0.0047$ ms/km. Likewise, few seismic events recorded at station TV11 seem to present an unusual behavior from a distance of 3.5 km, where the highest normalized delay time is $\delta t_n = 16.3$ ms/km, while a mean with a 95% confidence level is $\delta t_n = 7.1 \pm 0.0036$ ms/km.

Strength of anisotropy and main pathways

In the TVVC, high individual values of δt and A reaching up to 0.1616 s and 10.03%, respectively, indicate a high fracturing degree similar to results from other geothermal zones (e.g., 18.0% at the Takinoue geothermal area in Japan, Kaneshima et al. 1988; 7.0% at Uturuncu Volcano in Bolivia, Maher and Kendall 2018; 10.0% at Aluto Volcano in Ethiopia, Nowacki et al. 2018). The mean values of all δt and A data (MDT and MAP) were 0.0425 s and 1.823%, respectively (Fig. 5). The highest MDT value was 0.0587 s at station TV21 (Table 2; Fig. 3), while the highest MAP value was 2.53% at stations TV11 and TV18 (Table 3; Fig. 4), which are below the 4.5% limit proposed by Crampin and Leary (1993) and Crampin (1994) to differentiate between a low (below limit) and a high (above limit) fracture density. Thus, the variation range of the MAP values, 2.53 to 0.54% (lowest and highest levels), also indicates the existence from intermediate to low degree of fracturing in some areas (see Figs. 4 and 5).

Fig. 12 Delay times vs. f$_{max}$ and percentage of anisotropy vs. shear-wave velocities for seismic waveforms with a starting depth between 4.0 and 5.0 km (**a** and **b**) and for seismic waveforms with a starting depth between 5.0 and 6.0 km (**c** and **d**), which were recorded at stations TV01, TV03, TV04, TV011, and TV18 during 2010
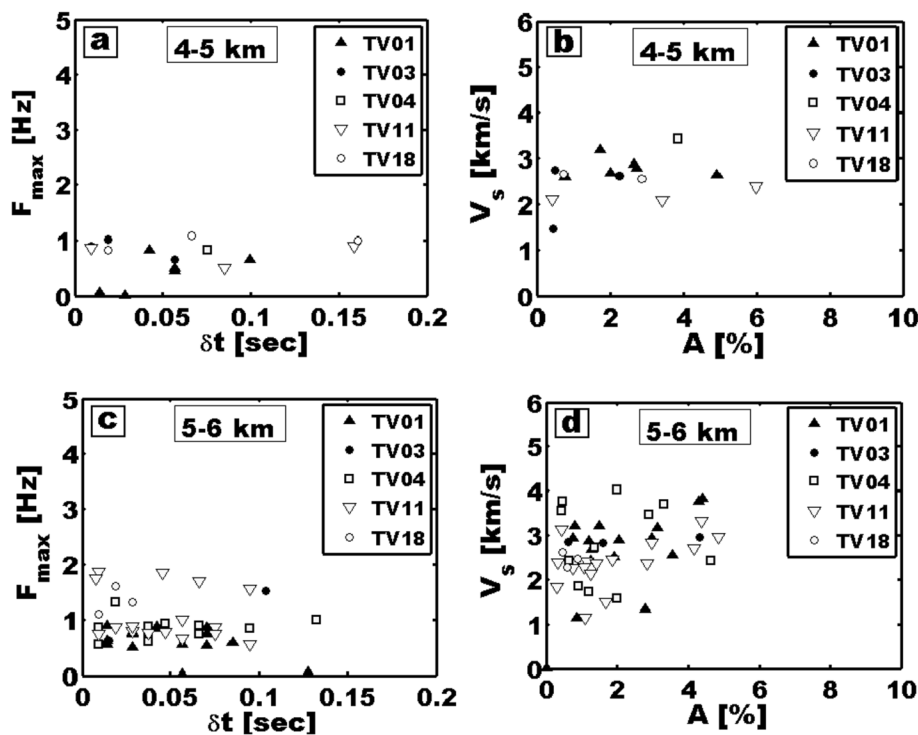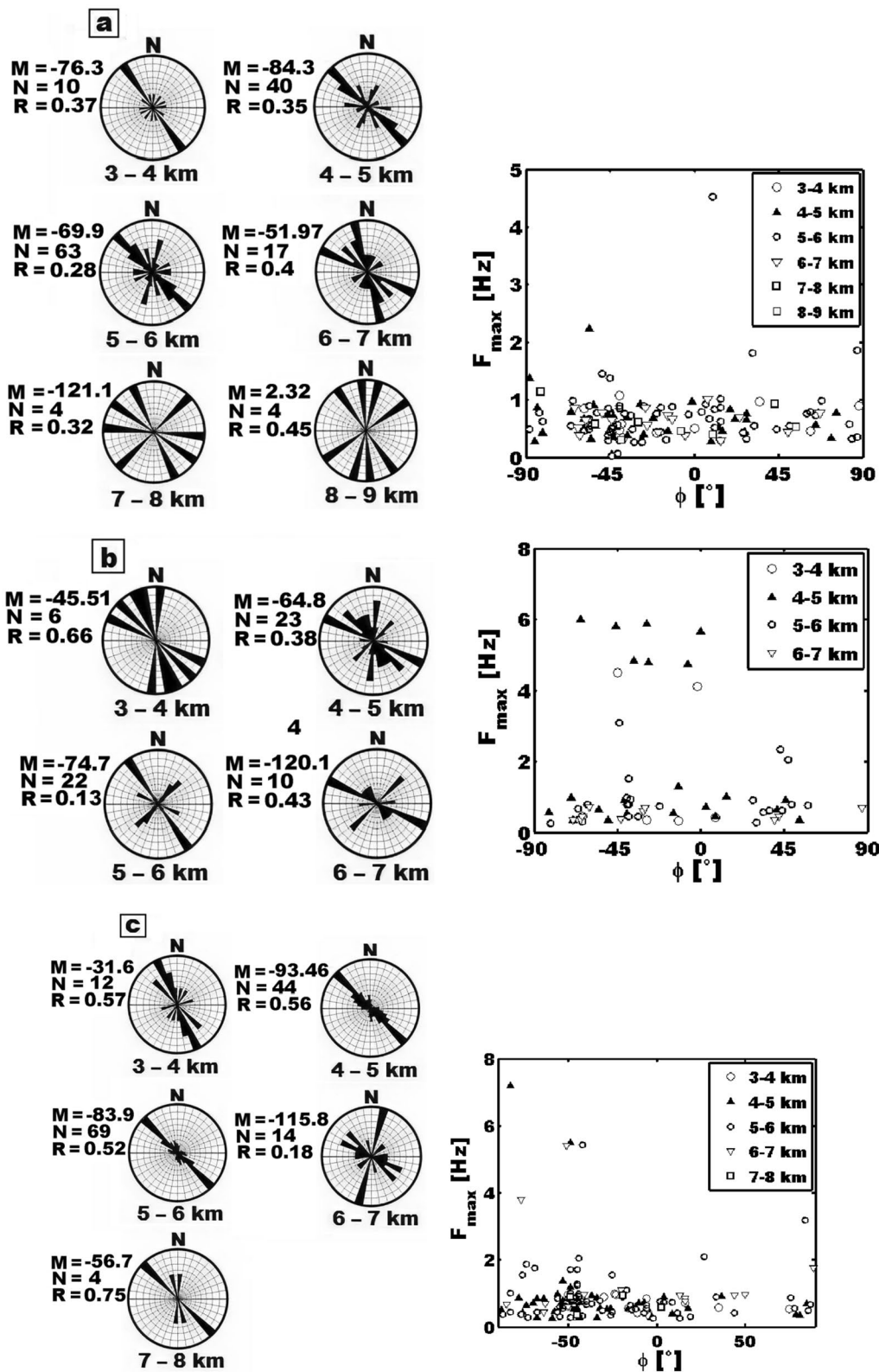
Fig. 13 Fast polarizations vs. depths analyzed for stations TV01 **a**, TV03 **b**, TV11 **c**, y TV18 **d**. The rose diagrams were elaborated using a bin size of 10° and a normalization of the polarizations with respect to the preferential direction. The total number of measurements N, the mean fast direction M, and the mean resultant length R are shown on each diagram. To the right are displayed the plots of φ vs. f_max for all depths and years obtained from events recorded at stations TV01, TV03, TV011, and TV18
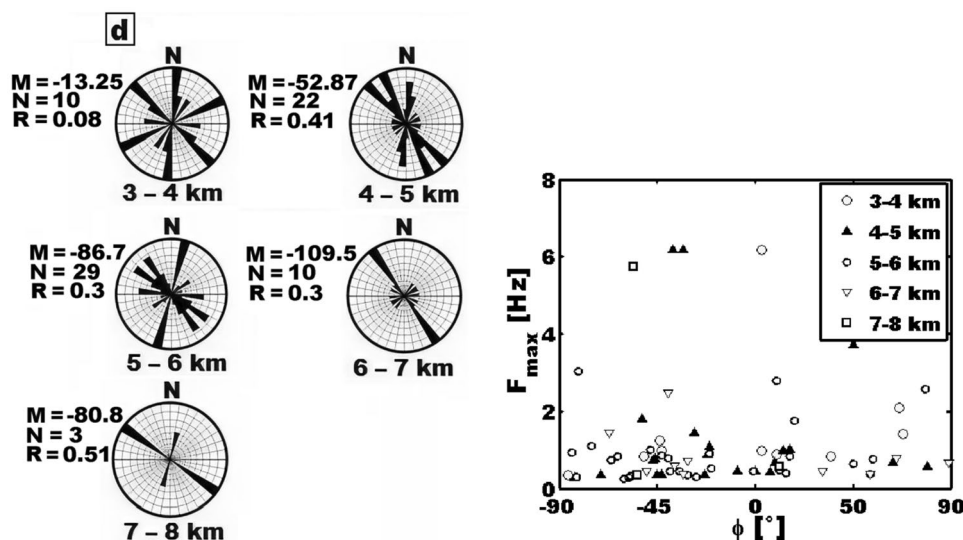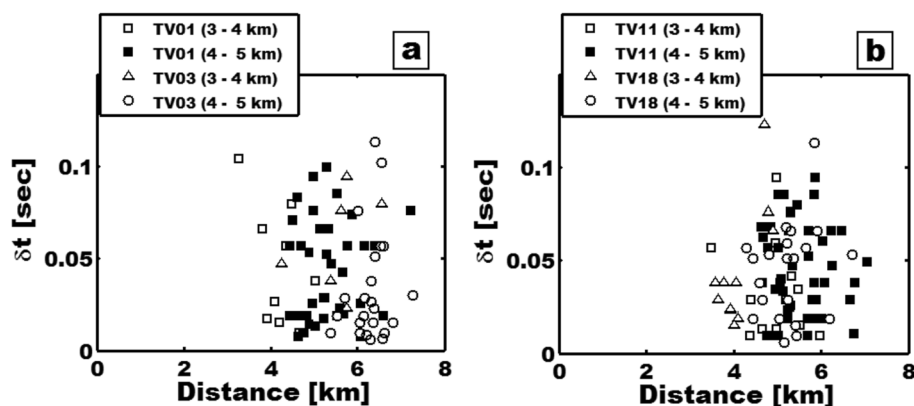
Fig. 13 (continued)

Fig. 14 Shear-wave splitting delays vs. hypocentral seismic distances analyzed for stations TV01 and TV03 **a**, and for stations TV11 and TV18 **b**. Inside the keys in the boxes, the values in kilometers refer to the depth of the seismic events and not to the hypocentral distance

High anisotropy (A > 4.5%, Crampin 1994) is mainly located beneath EAV and EVV, following the El Azufre, El Volcán, EPO, EV1, EV2, and La Reforma faults as well as some minor faults perpendicular and sub-parallel to the La Reforma fault (see Figs. 6, 7 and 8). The hypocentral seismic depths are mainly located between 3.0 and 6.5 km (Figs. 5a, b, and 6). Other important fracturing zones are also observed near LVV and toward the La Virgen-El Campamento, El Volcán, and El Mezquital faults, with hypocentral seismic depths between 4.0 and 6.0 km (Figs. 6 and 7). These anisotropic pathways delimit fracturing zone approximating conical shapes delimited by the pathways with vertices at stations TV01, TV04, TV11, and TV18, which can be observed at different depth levels depending on the origin of the seismic events analyzed (see Figs. 7a, 8c, d, e, f, and g). The conical shapes are not an intrinsic property but a product of the observation geometry (where the vertices are constituted by the seismic stations and the base is delineated by the hypocenters). Large fracturing is observed in a band around

the La Reforma–El Azufre fault system, between stations TV01 and TV18 (Figs. 6, 7c, d, and 8a), where anisotropic pathways intersect in a depth range of approximately 2.0 to 5.0 km (see Fig. 7c). These intersections present a horizontal extension that could reach approximately up to 2.5 km between both stations (see Fig. 7b). Between stations TV11 and TV18, anisotropic pathways also intersect in a depth range of approximately 2.0 to 5.0 km, but closer to TV18 (see Fig. 7d), with a horizontal extension that could reach approximately up to 3.0 km (see Fig. 7b). Another zone is located in the southern front of EVV and EAV. The last one delineates a band along the EV2 Fault, near station TV04 (Fig. 7c) and where geothermal wells are located (Fig. 7b).

The areas with high fracturing correlate with the main NW–SE fault systems, which reach down to 8.0 km in depth (see Fig. 13), and are controlled by NW–SE regional fracture systems as mentioned by Chacón-Hernández et al. (2021a) (i.e., the El Azufre, La Reforma, El Volcan, EV1, EV2 and EPO faults), which are parallel or sub-parallel to

the California Gulf transpression direction. This depth range is mainly located inside the plutonic rocks of the Peninsular Ranges Batholitic (Gastil et al. 1975), whose top has been observed at a depth of 1.13 km below the surface (e.g., Garduño-Monroy et al. 1993). The highest δt and A values indicate that from the upper part of the granitic basement (PRB unit, Fig. 8a) there are high degrees of fracturing. These high degrees of fracturing also span the shallowest geological units (i.e., SL-SF, EB, Ag, LVdld, Pdld, and UVdld, see Table 4, Fig. 8a, b, and c), which are strongly affected by the exploitation of the geothermal site and by natural hydrothermal phenomena, generating stratums with pervasive fracturing that take place from at least 3.5 and 4.5 km in areas near to stations TV01, TV11, and TV18 (see Fig. 14).

Inference of fluid saturations and magmatic bodies with respect to depth

Fluid flow in fracture systems linked to hydrothermal phenomena or geothermal activities has been observed to facilitate coalescence, growth of cracks, and fault activations [e.g., in geothermal environments (Vlahovic et al. 2002; Main et al. 1990; Clarke et al. 2019), and their effects are being assessed in theoretical equivalent models, Maultzsch et al. 2003; Chapman et al. 2003]. Since TVVC presents both hydrothermalism and geothermal activity, an analysis between δt and f_{max} values was conducted along with the analysis of the V_s and A values to discriminate fluid saturation degrees in fracture systems. According to previous works (van Der Kolk et al. 2001, Liu et al. 2001; Liu et al. 2003; Kozlov 2004), the data of the GA1 group can indicate intermediate and large fracturing levels with a lower effect of fluid content, which contrasts to the data of the GA2 group (e.g., in previous works, Chesnokov et al. 2001; Liu et al. 2001; Kozlov 2007). Seismic events of both groups were recorded at five stations (i.e., the TV01, TV03, TV04, TV11, and TV18 stations), located around EVV and EAV, with a depth range from 3.6 to 6.8 km for the GA1 group and from 3.5 to 6.0 km for the GA2 group. For the GA1 group, the seismic events recorded at the TV03 station presented a narrower depth range (from 4.6 to 5.1 km). Some of the hypocentral data of the GA1 group also form part of the GC3 group, mainly those events recorded at stations TV01 and TV04, where a narrower depth range from 5.0 to 6.0 km was observed at station TV04. These relationships between some data of the GA1 and GC3 groups would imply intermediate and large fracturing levels, which could probably indicate fractures with lower fluid content, whereby higher V_s values are observed (i.e., between 3.0 and 4.0 km/s, Fig. 10c).

The origin of seismic events analyzed in the GA2 group also present intermediate and large ranges of δt values but a higher range of f_{max} values (i.e., above 1.0 Hz), which according to studies of Elkibbi (2004) and Rial et al.

(2005) could be reflecting fracture systems under effects of higher fluid content or steam flow, whose V_s values present a decreasing from 3.6 to 1.5 km/s. The origin of seismic events analyzed in the GA2 group is located in a depth range between 3.5 and 6.0 km, but for stations TV03, TV04, and TV11, a narrower depth range was observed, mainly between 5.0 and 6.0 km (some seismic data are emphasized in the GC2 group) (see Table 5). This last depth range correlates with the 5–6-km depth interval of Figs. 12a and c, where higher f_{max} values were observed in some data, probably indicating a higher fluid content in fracture systems (e.g., for the GC2 group, V_s values range approximately between 2.0 and 3.4 km/s in some seismic data of stations TV11 and TV18), compared to the 4–5-km depth interval. This evidences variations in fluid contents from one depth interval to another in some areas, where probably the influence of geothermal activities is stronger in the 4–5-km depth interval and shallower depths, along with hydrothermalism phenomenon. A seismic tomography study conducted by Vilchis-García et al. (2019) considered compressional velocities $V_P < 4.25$ km/s and a ratio of $V_p/V_s < 1.75$ km/s in a depth less than 4.0 km as a combination of fluids and gases in a caprock. Meanwhile, $V_p/V_s > 1.75$ km/s in deeper zones than 4.0 km was related to fluid saturation in rocks and probably cold magma crystalized. These results correlate to some extent with what was observed in our analyses.

Fracture systems chemically sealed or impermeable sealing caps have been observed in geothermal areas (e.g., The Coso Range, Vlahovic et al. 2002; Los Humeros, Arzate et al. 2018). In the TVVC area, Portugal et al. (2000) verified the existence of sealed fractures, which could be indicated by some data of the GA3 group, characterized by low δt values (e.g., δt values from 0.005 to 0.02 s) and f_{max} values from 0.5 to 2.0 Hz (see Fig. 10a). This is according to previous works that related sealed fractures with decreases in dominant S-wave frequencies (e.g., Latter 1981; Zhao et al. 2002). Areas with these features are mainly located to the west of EAV and EVV and to the south of EAV (see Fig. 11a) where the depth ranges of the analyzed events go from 4.1 to 6.0 km. The seismic events analyzed for the GA3 group were recorded in all stations (see Fig. 10a), but in stations TV04 and TV18 they presented narrower depth ranges (from 5.5 to 6.0 and from 4.9 to 5.3 km, see Table 5).

Changes in fast polarization directions at certain locations and depths are interpreted as indicating fracture systems in other orientations (e.g., Fig. 13), but they could also be due to the presence of magmatic intrusion systems or subvolcanic bodies. This is because the magmatic phenomena are capable of modifying the orientations of fractures in the rock volume (e.g., the 90° flip effect) by changes in the local stress field as has been considered in other previous works (e.g., Roman et al. 2011; Baird et al. 2015; Maher and Kendall 2018). Thus, the presence of important N–S,

NE–SW, and E–W secondary polarizations observed for seismic events at deeper levels (e.g., depths ranges from 5.0 to 6.0 km at station TV01, Fig. 13a; depths > 4.0 km at station TV03, Fig. 13b; depths > 6.0 km at station TV11, Fig. 13c; depths > 5.0 km at station TV18, Fig. 13d) could be associated to magmatic phenomena.

The analysis between V_s and A values and between V_s and f_{max} values could support the presence of magmatic intrusion in the case of a correlation of the lowest V_s (from 1.0 to 2.5 km/s), A (from 0.1 to 2.5%, see Fig. 10b), and f_{max} values (lower than 1.0 Hz, see Fig. 10c) (i.e., some seismic data of the GB1 and GC1 groups). This is because, magmatic and volcanic phenomena reduce the V_s values (Vanorio et al. 2005), affecting the frequency contents and fast polarizations under conditions of high pore-fluid pressures (Crampin and Zatsepin 1997). These particular conditions are mainly found around EVV and EAV and near the TV01, TV04, and TV11 stations, related with the seismic events analyzed in the GB1 group for a focal depth range from 4.0 to 7.0 km (see Fig. 11 and Table 5) and in the seismic events analyzed in the GC1 group for a depth range from 4.4 to 6.0 km, with narrower depth ranges at stations TV01 and TV04 (from 5.1 to 5.7 and from 5.0 to 5.7 km, respectively, see Fig. 11 and Table 5). These depth ranges in the

GB1 and GC1 groups could be correlated with the 5–6-km depth interval observed in Fig. 12d, mainly for some events recorded at station TV01, TV04, and TV11 with lower V_s and A values. In previous studies of seismic tomography (e.g., $V_P > 4.25$ km/s and $V_P/V_S > 1.75$ km/s in zones deeper than 4.0 km, Vilchis-García et al. 2019), inversion of aeromagnetic data (magnetic sources in a depth range from 4.5 to 8.0 km, Avellán et al. 2019), and *b* value (*b* values between 1.1 and 1.5 for a range depth from 4.0 to 6.0 km, Antayhua-Vera et al. 2022) have also considered the presence of magmatic bodies, crystallized magma, or the emplacement of magmatic bodies (i.e., dikes).

Table 6 summarizes depths at which low, intermediate, and high fracturing zones are located together with their inferred different fluid contents. It also indicates the initial depths of pervasive anisotropy, as well as the possible presence of magmatic bodies. Figure 15 shows, in a conceptual sketch, the distribution of highly anisotropic rock volumes and the respective phenomena and processes interpreted to be their causes beneath the TVVC. Most of the main fault systems, that follow the regional stress and correlate with the fast polarization results (e.g., Fig. 13; see Chacón-Hernández et al. 2021a), cannot entirely explain the upper crustal anisotropy observed at the TVVC. Thus, the distribution,

Table 6 Summary the different phenomena that could be occurring in the TVVC at different depth levels. Phenomena occurring in certain depth ranges are also specified, indicating in parentheses the stations for which the seismic data were analyzed. All stations mean the TV01, TV03, TV04, TV11, and TV18 stations

Depth intervals [km]	Pervasive anisotropy	High fracturing with lower fluid content	High fracturing with higher fluid content	Intermediate fracturing with lower and higher fluid content	Sealed fractures	Magmatic influences
General range (All stations)	–	3.5–6.8 km	3.5–6.0 km	3.5–6.8 km (considering the GA1 and GA2 groups)	4.1–6.0 km	–
Particular depth intervals < 3 (km)	–	–	–	–	–	–
3–4 (km)	< 3.5 (TV01 and TV11)		–	–	–	–
4–5 (km)	< 4.5 (TV18)	GA1 group 4.6–5.1 (TV03)		–		Rose diagrams > 4.0 (TV03)
5–6 (km)	–	GC3 group 5.0–6.0 (TV04)	GA2 group Some data from the GC2 group 5.5 (TV04) 5.5–6.0 (TV03) 5.5–6.0 (TV03) 5.0–5.2 (TV11) 5.0–5.2 (TV11)	–	GA3 group 4.9–5-3 (TV18) 5.5–6.0 (TV04) 5.5–6.0 (TV04)	Rose diagrams 5–6 (TV01) > 5.0 (TV18) GC1 group 5.1–5.7 (TV01) 5.0–5.7 (TV04)
> 6 (km)	–	–	–	–	–	Rose diagram > 6.0 (TV11)

Fig. 15 A general sketch of the TVVC area showing the distribution of high anisotropic volumes influenced by different phenomena and processes occurring at different depths. The planes cutting the volume beneath the TVVC represent the zones featured by the following fault systems: (1) La Reforma, (2) El Volcán, (3) La Virgen-El Campamento, and (4) El Mezquital. σ_H represents the main regional horizontal stress field related to the Gulf of California opening with a NW–SE direction. The white spheres represent earthquakes hypocenters for the years of 2011–2013, while the black spheres are related only for 2010, which were considered in the analyses represented in Figs. 10, 11, and 12.
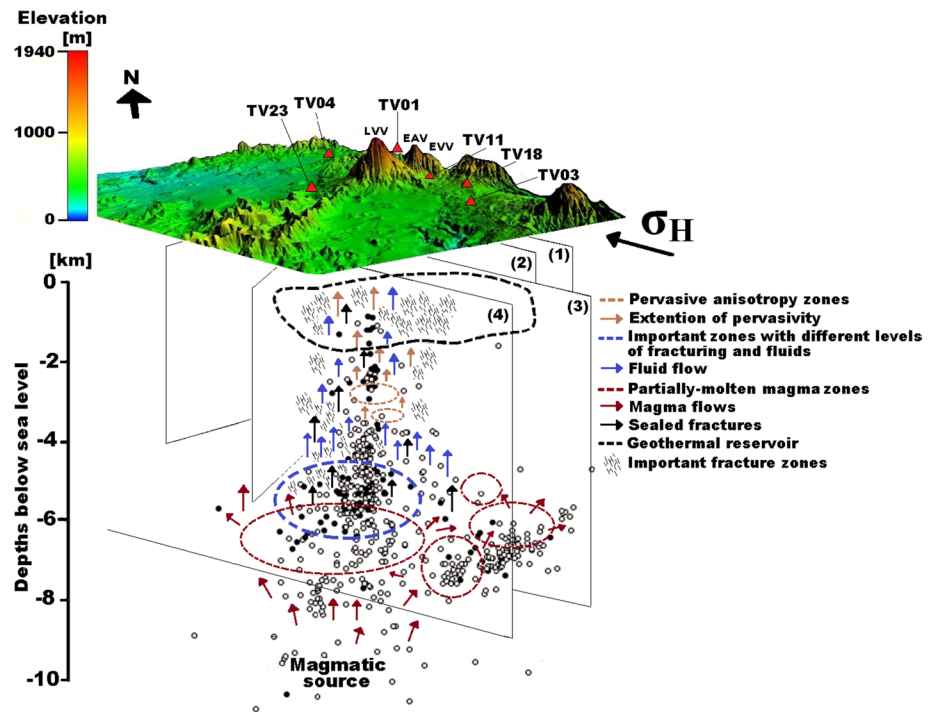
both vertically as across the TVVC, of the fracturing degree zones and their fluid content is uneven, but the distribution of high fracturing zones with high, intermediate, and low fluid content tends to start at least beneath 6.0 km depth (Figs. 5, 6, 7, 8 and 11, and Table 5) and extends toward the surface (e.g., the areas with the dashed blue lines and the distribution of the blue arrows, Fig. 15). The associated large anisotropy percentage implies that the rock volumes are essentially cracked and fractured, and in an unstable state due to high pore-pressures and/or fluid-filled cracks. In zones deeper than 6 km, the higher pressure and temperature conditions would indicate that fluids hosted in cracked volumes are in a super-critical state.

At shallower depths, there are also fractured zones with high fluid content and under high confining pressures linked to hydrothermal and geothermal processes that can generate cracks opening. Strata with pervasive anisotropy can be considered to begin at a 3.5-km depth for seismic data registered at stations TV01 and TV11, but at a 4.5 km depth for data recorded at station TV18 (high values of anisotropy and normalized delay times, Figs. 5b and 14), which correlates with the highest fracture concentrations and important permeable zones. These zones allow feeding the geothermal reservoir (e.g., see areas outlined with dashed brown lines and brown arrow distributions spanning up to the geothermal reservoir outlined by dashed black lines, Fig. 15) with gas-rich fluid overpressure from multiple fracture sets (i.e., by convection and advection processes; blue and red arrows in Fig. 15), which are heated by magmatic bodies. These zones are delineated approximately by means of the

density of established anisotropy pathway (i.e., stations TV01, TV11, and TV18, Figs. 7 and 8) at depths between 2.0 and 5.0 km and from 2.0 to 5.0 km in the case of data registered at stations TV11 and TV18. Nonetheless, on the other hand, low fracturing could also be considered (e.g., low anisotropy values and normalized delay times, Figs. 5b and 14) due to small confining pressures (e.g., Piccinini and Saccorotti 2018); while in deeper areas, it could be related to over-pressurized hydraulic compartments with pore fluids undispersed (Crampin and Leary 1993). Furthermore, at several depths, due to chemical processes, there would be the existence of sealed fractures (e.g., see black arrows above 3 km, Fig. 15).

For seismic sources events recorded at stations TV03, TV01, TV18, and TV11 at respective depths below levels of 4.0, 5.0, and 6.0 km, not only NW–SE fast directions are observed, but also orthogonal fast directions for seismic sources in spatial ranges constrained as similarly to previous works (e.g., Piccinini and Saccorotti 2018). These effects are particularly observed in proximity of the La Reforma and El Volcan faults. Both fault systems comprise important pathways for the up flow of magmatic fluids from depth. These orthogonal polarizations could evidence the presence of heavily fractured rocks at critically high pore-fluid pressures (e.g., Crampin and Zatsepin 1997) generated by geothermal operations, hydrothermalism (e.g., Pinel and Jaupart 2003; Muirhead et al. 2015), or magmatic fluxes (e.g., Nowacky et al. 2018) (see the areas with the dashed red lines and the distribution of the red arrows, Fig. 15), phenomena that can give rise to differential stresses.

These different saturated fluid contents, sealed fracture effects, and magmatic intrusions occur at the upper part of the granitic basement (the PRB geological unit, Fig. 8a) and reach superficial zones, crossing mainly shallow units (e.g., the SL-SF, EB, Ag, LVdld, Pdld, and UVdld units). The concurrence of these phenomena is related to volcanic environment along with geothermal phenomena that have potential to provide geothermal energy in zones with high fracture densities (e.g., anisotropic pathways delineating conical shapes due to the different arrival angles with vertices at stations, Figs. 7 and 8), which affect the different lithological units. This appears to be mainly located in and around the volcanic zones (see Fig. 11). When these volcanic phenomena and geothermal processes act under a state of continuous stress, they may generate deformation cycles in and around the TVVC area. For instance, NE–SW and N–S secondary fracture sets with different orientations to the pre-existing NW–SE fault structures parallel or sub-parallel orientation to the Gulf of California opening (i.e., the main regional horizontal stress field σ_H, Chacón-Hernández et al. 2021a, b) could be created, with damage in the rock volume associated with these structures. At shallower depths, high fracturing zones (i.e., large A values associated) indicate structural weakness and would allow generating surface deformations easily, with pre-existing structures controlling the hydrothermal systems as could be occurring around the TVVC area and in other areas (e.g., at the Aluto Volcano, Nowacky et al. 2018). However, at greater depths (e.g., > 5.0 km), as any NW–SE fractures would need to be held open by fluids at high pore-fluid pressures, even away from the geothermal system, the main deformation could be related to strong overpressure fluids linked to magmatic fluids. Thus, if multiple fracture sets are present in the presence of a regional stress field, only one set would be held open. Therefore, over-pressurized fluids are present beneath the volcanic complex, and the overpressure is sufficient to hold open both fracture sets (e.g., secondary directions in rose diagrams, Fig. 13).

Conclusions

The main contributions to the characterization of some zones in the TVVC area are:

(1) Shear-wave splitting delays and the anisotropy percentage provided information about the highest fractured zones and their most important anisotropic pathways, which delineate conical shapes with vertices at the stations TV01, TV04, TV11, and TV18. These conical shapes delimit portions of important volumes of fractured rocks, which are mainly located in the vol-

canic region between EVV and EAV, and toward the La Reforma, El Azufre, El Volcán, EPO, EV1, and EV2 faults. They intersect between stations TV01 and TV18, with a depth range from approximately 2.0 to 5.0 km and with a horizontal extension of approximately 2.5 km between both stations. Likewise, anisotropic pathways intersect between stations TV11 and TV18, with a range from approximately 2.0 to 5.0 km in depth and with an extension of approximately 2.5 km in a straight line between both stations. These zones represent important permeable-fractured zones and can be considered to expand the geothermal exploitation of the geothermal resources, strengthening the analyses of previous studies (e.g., hydrothermal characterization, Romo-Jones et al. 2018; evaluation of geothermal potential, Tello-López and Torres-Rodríguez 2015; fluid inclusion in fractured rocks (temperatures higher than 240 °C at depths between 1.5 and 2.5 km in the TVVC), Romo-Jones et al. 2000; Wong et al. 2001) and helping to describe the existence of new permeable rock volumes. Additionally, some other external areas with high fracturing are also observed near the LVV volcano and toward the La Virgen-El Campamento, El Volcán, and El Mezquital faults. These high fracturing zones reached the upper part of the PRB geological basement whose top has been observed at a depth of 1.13 km below the surface (Garduño-Monroy et al. 1993), and it includes the shallowest geological units (SL-SF, EB, Ag, LVdld, Pdld, and UVdld among others), where the geothermal reservoir has been considered to be located at depths of around 1.5 km.

(2) The selection of seismic events near stations (i.e., < 0.035° in latitude and longitude) and restricted to specific areas with incident angles less than 45°, enabled to assure as much as possible homogeneous conditions of some factors and phenomena that affect the anisotropic signals (i.e., rock and lithology types, fracture orientations, fluid inclusions, magmatic influences, or particular fault systems). This constraint on the data enables us to observe a pervasive anisotropy near the TV01 (i.e., δt $n = 31.95$ ms/km), TV11 (i.e., δt $n = 16.3$ ms/km), and TV18 (i.e., δt $n = 26.17$ ms/km) stations with a hypocentral distance from at least 3.5 and 4.0 km.

(3) The relationships observed between values of δt vs. f_{max}, A vs. V_s, and f_{max} vs. V_s allow considering the possibility that fracture systems could be affected by different fluid content, steam flow, or that they have been chemically sealed. These circumstances do not seem to constitute a feature of a unique zone and depth, as is evidenced by the different values of each data group GA1, GA2, GA3, GB1, GC1, GC2, and GC3

(see Fig. 11 and Table 5). For instance, larger fluid content could be mostly considered in the 5–6-km depth interval for those data related to station TV11 compared with the 4–5-km depth interval, which is supported by the different f_{max} and V_s values (e.g., Fig. 12).

(4) The analysis of the main fast polarization directions with respect to the different depth ranges of the analyzed seismic events, allowed considering a strong NW–SE regional fracture system reaching a minimal depth of 8.0 km, accompanied by minor NE–SW, NNE–SSW, N–S, or E–W fracture systems which could be representing intersection of fracture systems. In general, it was possible to observe that fracture systems contribute to the anisotropy observed at different depth levels.

(5) Noteworthy variations of fast polarizations observed in the rose diagrams, preferentially for those seismic events analyzed deeper than 4–5 km at station TV03, 5–6 km at stations TV01 and TV18, and deeper than 6.0 km at station TV11, indicate fracture systems in other orientations, which could be due to the influence of magmatic bodies, intrusive systems or subvolcanic bodies, whose depths seem to be correlated with those reported in other previous studies. The presence of magmatic bodies could be supported by lower f_{max}, A, and V_s, values (i.e., groups GB1 and GC1), which seem to be located from the 4.0 km depth (e.g., for the seismic events recorded at station TV01 of the GB1 group, Table 5) but more concentrated from the 5–6 km depth interval and around EVV and EAV. It must be stated that the location of possible magmatic bodies does not necessarily follow a single depth interval with homogeneous effects, but in different places and depths.

(6) Our results indicate that anisotropy is being affected by volcanic and geothermal processes, representing multifaceted effects operating throughout different places and depths, where different fluid contents, steam flow, and magmatic bodies could be occurring and interacting at a same depth interval. Likewise, this study evidences a structurally complex and highly fractured area, at least in the zone of EVV and EAV and toward the La Reforma, El Azufre, El Mezquital, El Volcán, EPO, EV1, and EV2 faults, which evolve as volcanic and geothermal processes continue generating changes in the local stress field.

Declarations

References

Ando M, Ishikawa Y, Wada H (1980) S-wave anisotropy in the upper mantle under a volcanic area in Japan. Nature 286:43–46

Angerer E, Crampin S, Li X-Y, Davis TL (2002) Processing, modelling and predicting time-lapse effects of overpressured fluid-injection in a fractured reservoir. Geophys J Int 149(2):267–280. https://doi.org/10.1046/j.1365-246X.2002.01607.x

Antayhua-Vera YT, Zuñiga FR, Lermo-Samaniego J, Campos-Enríquez JO, Quintanar-Robles L (2022) Spatio-temporal distribution of the b-value in the volcanic complex and geothermal field of Tres Vírgenes; Baja California Sur, Mexico. J S Am Earth Sci 116:103864

Arzate J, Corbo-Camargo F, Carrasco-Núñez G, Hernández J, Yutsis V (2018) The Los Humeros (Mexico) geothermal field model deduced from new geophysical and geological data. Geothermics 71:200–211. https://doi.org/10.1016/j.geothermics.2017.09.009

Atwater T (1989) Plate tectonic history of the northeast Pacific and western North America. In: Winterer EL, Hussong DM, Decker RW (eds) The eastern Pacific Ocean and Hawaii. Geological Society of America, North America, pp 21–72. https://doi.org/10.1130/DNAG-GNA-N.21

Audoine E, Savage MK, Gledhill K (2004) Anisotropic structure under a back arc spreading region, the Taupo Volcanic Zone, New Zealand. J Geophys Res Solid Earth. https://doi.org/10.1029/2003JB002932

Avellán DR, Macías JL, Arce JL, Jiménez-Haro A, Saucedo-Girón R, Garduño-Monroy VH, Layer PW (2018) Eruptive chronology and tectonic context of the late Pleistocene Tres Vírgenes volcanic complex, Baja California Sur (México). J Volcanol Geothermal Res 360:100–125

Avellán DR, Macías JL, Arce JL, Saucedo-Girón R, Garduño-Monroy VH, Jiménez-Haro A, Sosa-Ceballos G, Cisneros G, Bernal JP, Layer PW, García-Sánchez L, Reyes-Agustín G, Rangel E, Navarrete JA, López-Loera H (2019) Geology of the late Pleistocene Tres Vírgenes Volcanic Complex, Baja California Sur (México). J Maps 15(2):227–237. https://doi.org/10.1080/17445647.2019.1576552

Baird AF, Kendall JM, Sparks RSJ, Baptie B (2015) Transtensional deformation of Montserrat revealed by shear wave splitting.

Earth Planet Sci Lett 425:179–186. https://doi.org/10.1016/j.epsl.2015.06.006

Benton A, García F, Silis J, Cruz S, (2011) Estudio geohidrológico de la cuenca de Tres Vírgenes, B.C.S., Gerencia de proyectos Geotermoeléctricos, Comisón Federal de Electricidad, Informe DEX-DGL-TV-16–11, pp 196

Berens P (2009) CircStat: a MATLAB toolbox for circular statistics. J Stat Softw 31(10):1–21

Bonini M, Cerca M, Moratti G, López-Martínez M, Corti G, Gracia-Marroquín D (2019) Strain partitioning in highly oblique rift settings: Inferences from the southwestern margin of the Gulf of California (Baja California Sur Mexico). Tectonics, México. https://doi.org/10.1029/2019TC005566

Booth DC, Crampin S (1985) Shear-wave polarizations on a curved wavefront at an isotropic free-surface. Geophys J R Astron Soc 83:31–45

Bowman R, Ando M (1987) Shear wave splitting in the upper mantle wedge above the Tonga subduction zone. Geophys J R 88:25–41

Campos-Enríquez JO (1992) Geophysical prospecting for geothermal resources in Mexico. Geofís Int 31(4):339–340

Campos-Enríquez JO, Espinosa-Cardeña JM, Oksum E (2019) Subduction control on the curie isotherm around the Pacific-North America plate boundary in northwestern Mexico (Gulf of California). Preliminary results. J Volcanol Geoth Res 375:1–17

Chacón-Hernández F, Zúñiga FR, Campos-Enríquez JO, Lermo-Samaniego J, Jiménez-Méndez N (2021a) Analysis of shear wave splitting anisotropy in the Tres Virgenes Volcanic Complex, Baja California Sur Mexico. Geothermics 94:102115

Chacón-Hernández F, Zúñiga FR, Lermo-Samaniego J, Jiménez-Méndez N (2021b) Analysis of shear wave splitting parameters in los Humeros geothermal field, Puebla, Mexico. J Volcanol Geothermal Res 413:107210. https://doi.org/10.1016/j.jvolgeores.2021.107210

Chapman M (2003) Frequency-dependent anisotropy due to meso-scale fractures in the presence of equant porosity. Geophys Prospect 51(5):369–379

Chapman M, Maultzsch S, Liu E, Li XY (2003) The effect of fluid saturation in an anisotropic multi-scale equant porosity model. J Appl Geophys 54(3–4):191–202

Chesnokov EM, Queen JH, Vichorev A, Lynn HB, Hooper J, Bayuk I, Castagna J, Roy B, (2001) Frequency-dependent anisotropy, Expanded Abstracts, 71st Ann. Int. SEG Mtng., pp 125

Clarke H, Verdon JP, Kettlety T, Baird AF, Kendall JM (2019) Real-time imaging, forecasting, and management of human-induced seismicity at Preston New Road, Lancashire, England. Seismol Res Lett 90(5):1902–1915

Coletta B, Angelier J, (1981) Faulting evolution of Santa Rosalia Basin, Baja California Sur, Mexico. In: Ortlieb L, Roldan JE, Portugal et al. Journal Volcanology and Geothermal Research 101 (2000) 223–244 242 (Eds.), Field Guides and Papers: Geology of Northwestern and Southern Arizona, pp 265–274

Conly AG, Brenan JM, Bellon H, Scott SD (2005) Arc to rift transitional volcanism in the Santa Rosalía Region, Baja California Sur, Mexico. J Volcanol Geotherm Res 142:303–341. https://doi.org/10.1016/j.jvolgeores.2004.11.013

Crampin S (1994) The fracture criticality of crustal rocks. Geophys J Int 118:428–438. https://doi.org/10.1111/j.1365-246X.1994.tb03974.x

Crampin S, Zatsepin V (1997) Modelling the compliance of crustal rock-II. Response to temporal changes before earthquakes. Geophys J Int 129(3):495–506. https://doi.org/10.1111/j.1365-246X.1997.tb04489.x

Crampin S, Leary PC, (1993) Limits to crack density: the state of fractures in crustal rocks. In: SEG Technical Program Expanded Abstracts 1993. Society of Exploration Geophysicists. pp 758–761

Demant, A., 1981. Plio-Quaternary volcanism of the Santa Rosalia area, Baja California, Mexico. In: Ortlieb, L., Roldan, J. (Eds.), Geology of Northwestern Mexico and Southern Mexico and Sourhern Arizon. Field Guides and Papers, pp 295–307

Demant, A., 1984. The Reforma caldera, Santa Rosalia area, Baja California. A volcanical, petrological and mineralogical study, In: Malpica-Cruz, V., Celis-Guterrez, S., Guerrero-García, J., Ortlieb, L. (Eds), Neotectoniccs and sea level variations in the Gulf of California area, Symposium (Hermosillo, Son., April), pp. 21–23.

Elkibbi M (2004) Characterization of fracture-induced anisotropy using shear-wave splitting in The Geysers reservoir, California, PhD dissertation, University of North Carolina, Chapel Hill, NC

Ellsworth WL (2013) Injection-induced earthquakes. Science 341(6142):1225942

Erten, D., Elkibbi, M., Rial, J.A., 2001. Shear wave splitting and fracture pattern at the Geysers (California) geothermal field. In: 26th workshop on geothermal reservoir engineering, Stanford University

Evans R (1984) Effects of the free surface on shear wavetrains, Geophys. J.R. Astron Soc 76:165–172

Garduño-Monroy VH, Vargas-Ledezma H, Campos-Enríquez JO (1993) Preliminary geologic studies of Sierra El Aguajito (Baja California, Mexico): a resurgent-type caldera. J Volcanol Geoth Res 59(1–2):47–58

Gastil RG, Phillips RP, Allison EC (1975) Reconnaissance geology of the state of Baja California. Geol Soc Amer Mem 140:170. https://doi.org/10.1130/MEM140-p1

Gastil RG, Krummenacher D, Minch J (1979) The record of Cenozoic volcanism around the Gulf of California. Geol Soc Am Bull 90:839–857. https://doi.org/10.1130/0016-7606(1979)90%3C839:TROCVA%3E2.0.CO;2

Gerst A, Savage MK (2004) Seismic anisotropy beneath Ruapehu volcano: a possible eruption forecasting tool. Science 306(5701):1543–1547

Gledhill KR (1991) Evidence for shallow and pervasive seismic anisotropy in the Wellington region, New Zealand. J Geophys Res Solid Earth 96(B13):21503–21516

Gómez G, Rocha S, (2009) Estudio structural a detalle en la zona noreste y noroeste del campo geotérmico Las Tres vírgenes, B.C.S., Gerencia de Proyectos geotermoeléctricos, Subgerencia de Estudios, Comisión Federal de Electricidad,, Subgerencia de Estudios, DEX-DGL-TV-06–09, pp 52

Johnson JH, Savage MK, Townend J (2011) Distinguishing between stress-induced and structural anisotropy at Mount Ruapehu Volcano, New Zealand. J Geophys Res Solid Earth. https://doi.org/10.1029/2011JB008308

Kaneshima S, Ito H, Sugihara M (1988) Shear-wave splitting observed above small earthquakes in a geothermal area of Japan. Geophys J R Astron Soc 94:399–411

Kozlov E (2004) Pressure-dependent seismic response of fractured rock. Geophysics 69(4):885–897

Kozlov E (2007) Seismic signature of a permeable, dual-porosity layer. Geophysics 72(5):SM281–SM291

Latter JH (1981) Location of zones of anomalously high S-wave attenuation in the upper crust near Ruapehu and Ngauruhoe volcanoes, New Zealand. J Volcanol Geoth Res 10(1–3):125–156

Lermo J, Vargas A, Urban E, Rodríguez H, Núnez E, Espitia G, (2010) Estudio de sísmica pasiva en Las Tres Vírgenes, BCS, Periodo 2010. Instituto de Ingeniería, Universidad Nacional Autónoma de M' ixico, Gerencia de Proyectos Geotermoelectricos Departamento de Exploración, proyecto CFE-DEV-DGF-TV-25–10

Lermo J, Vargas A, Antayhua Y, Valseca R, Jiménez N, Torres Cuenca R, Ramon Perez E, (2014) Sísmica pasiva en el campo geotérmico Tres Vírgenes, BCS, Primer Informe técnico, Gerencia de Proyectos Geotermoelectricos, CFE

Liu E, Crampin S, Queen JH, Rizer WD (1993) Behaviour of shear waves in rocks with two sets of parallel cracks. Geophys J Int 113(2):509–517. https://doi.org/10.1111/j.1365-246X.1993.tb00903.x

Liu E, Hudson JA, Pointer T (2000) Equivalent medium representation of fractured rock. J Geophys Res 105(B2):2981–3000

Liu E, Queen JH, Li XY, Chapman M, Maultzsch S, Lynn HB, Chesnokov EM (2003) Observation and analysis of frequency-dependent anisotropy from a multicomponent VSP at Bluebell-Altamont field, Utah. J Appl Geophys 54(3–4):319–333

Liu K, Zhang Z, Hu J, Teng J (2001) Frequency band-dependence of S-wave splitting in China mainland and its implications. Sci China Ser D-Earth Sci 44:659–665

Lonsdale P (1991) Structural patterns of the Pacific floor offshore of Peninsular California, The Gulf and Peninsular Provinces of the Californias. In: Dauphine JP, Simoneit BRT (eds) The Gulf and Peninsular province of the Californias. The Gulf and Peninsular province of the Californias, Californias, pp 301–369

López-Hernández A, Casarrubias UZ, Leal HR, (1993) Estudio geológico regional de la zona geotérmica de Las Tres Virgenes, B.C.S. C.F.E. - G.P.G. internal report

López-Hernández A, Garcia-Estrada G, Arellano-Guadarrama F, (1995) Geothermal exploration at Las Tres Virgenes, B.C.S., Mexico. Gerencia de proyectos geotermoelectricos CFE

Lou M, Shalev E, Malin PE (1997) Shear-wave splitting and fracture alignments at the Northwest Geysers, California. Geophys Res Lett 24(15):1895–1898

Macias-Vásquez J-S (2012) Actualización vulcanológica del complejo de Las Tres Vírgenes, BCS. BCS Geotermia 26(1):26–28

Maher S, Kendall JM (2018) Crustal anisotropy and state of stress at Uturuncu Volcano, Bolivia, from shear-wave splitting measurements and magnitude–frequency distributions in seismicity. Earth Planet Sci Lett 495:38–49. https://doi.org/10.1016/j.epsl.2018.04.060

Main IG, Peacock S, Meredith PG (1990) Scattering attenuation and the fractal geometry of fracture systems. Pure Appl Geophys 133(2):283–304

Marson-Pidgeon K, Savage MK (1997) Frequency-dependent anisotropy in Wellington, New Zealand. Geophys Res Lett 24(24):3297–3300

Maultzsch S, Chapman M, Liu E, Li XY (2003) Modelling frequency-dependent seismic anisotropy in fluid-saturated rock with aligned fractures, implication of fracture size estimation from anisotropic measurements. Geophys Prospect 51:381–392

McGarr A, Simpson D, Seeber L, Lee W (2002) Case histories of induced and triggered seismicity. Int Geophys Series 81(A):647–664

Miller V, Savage M (2001) Changes in seismic anisotropy after volcanic eruptions: evidence from Mount Ruapehu. Science 293(5538):2231–2233

Mroczek S, Savage MK, Hopp C, Sewell SM (2020) Anisotropy as an indicator for reservoir changes: example from the Rotokawa and Ngatamariki geothermal fields, New Zealand. Geophys J Int 220(1):1–17

Muirhead JD, Kattenhorn SA, Le Corvec N (2015) Varying styles of magmatic strain accommodation across the East African Rift. Geochem Geophys Geosyst 16(8):2775–2795

Nowacki A, Wilks M, Kendall JM, Biggs J, Ayele A (2018) Characterising hydrothermal fluid pathways beneath Aluto volcano, Main Ethiopian Rift, using shear wave splitting. J Volcanol Geoth Res 356:331–341. https://doi.org/10.1016/j.jvolgeores.2018.03.023

Ottemöller L, Voss P, Havskov J, (2013) Seisan earthquake analysis software, version 10.0. pp 402

Peng Z, Ben-Zion Y (2004) Systematic analysis of crustal anisotropy along the Karadere—Düzce branch of the North Anatolian fault.

Geophys J Int 159(1):253–274. https://doi.org/10.1111/j.1365-246X.2004.02379

Piccinini D, Saccorotti G (2018) Observation and analyses of shear wave splitting at the Larderello-Travale geothermal field, Italy. J Volcanol Geoth Res 363:1–9

Pinel V, Jaupart C (2003) Magma chamber behavior beneath a volcanic edifice. J Geophys Res Solid Earth. https://doi.org/10.1029/2002JB001751

Portugal E, Birkle P, Tello E, Tello M (2000) Hydrochemical–isotopic and hydrogeological conceptual model of the Las Tres Vırgenes geothermal field, Baja California Sur, México. J Volcanol Geoth Res 101(3–4):223–244

Prol-Ledesma RM, Arango-Galvan C, Torres-Vera MA (2016) Rigorous analysis of available data from Cerro Prieto and Las Tres Vírgenes geothermal fields with calculations for expanded electricity generation. Nat Resour Res 25(4):445–458

Rial JA, Elkibbi M, Yang M (2005) Shear-wave splitting as a tool for the characterization of geothermal fractured reservoirs: lessons learned. Geothermics 34:365–385

Roman DC, Savage MK, Arnold R, Latchman JL, De Angelis S (2011) Analysis and forward modeling of seismic anisotropy during the ongoing eruption of the Soufrière Hills Volcano, Montserrat, 1996–2007. J Geophys Res Solid Earth. https://doi.org/10.1029/2010JB007667

Romo-Jones JM, Wong-Ortega V, Flores-Luna C, Vázquez-González R (2000) Conductividad eléctrica y atenuación de Ondas de Coda en el campo geotérmico las tres vírgenes en baja California Sur México. GEOS 20(1):21–29

Romo-Jones JM, Flores C, Vazquez R, (2018) The subsurface electrical conductivity and the attenuation of coda waves at Las Tres Vírgenes geothermal field in Baja California Sur, México

Rubinstein JL, Mahani AB (2015) Myths and facts on wastewater injection, hydraulic fracturing, enhanced oil recovery, and induced seismicity. Seismol Res Lett 86(4):1060–1067

Savage MK, Peppin WA, Vetter UR (1990) Shear wave anisotropy and stress direction in and near Long Valley caldera, California, 1979–1988. J Geophys Res Solid Earth 95(B7):11165–11177

Savage MK, Ohminato T, Aoki Y, Tsuji H, Greve SM (2010) Stress magnitude and its temporal variation at Mt. Asama Volcano, Japan, from seismic anisotropy and GPS. Earth Planetary Sci Lett 290(3–4):403–414

Sawlan MG, (1981) Late Cenozoic volcanism in the Tres Vírgenes area. In: Proceedings of the geology of northwestern Mexico and Southern Arizona. Congress. Universidad Nacional Autónoma México Hermosillo, Sonora, México, pp 309–319

Sayers CM, Schutjens PM (2007) An introduction to reservoir geomechanics. Lead Edge 26(5):597–601

Schutjens PMTM, Hanssen TH, Hettema MHH, Merour J, De Bree P, Coremans JWA, Helliesen G (2004) Compaction-induced porosity/permeability reduction in sandstone reservoirs: data and model for elasticity-dominated deformation. SPE Reservoir Eval Eng 7(03):202–216

Stock JM, Hodges KV (1989) Pre-Pliocene extension around the Gulf of California and the transfer of Baja California to the Pacific plate. Tectonics 8:99–115. https://doi.org/10.1029/TC008i001p00099

Tang C, Rial JA, Lees JM (2005) Shear-wave splitting: a diagnostic tool to monitor fluid pressure in geothermal fields. Geophys Res Lett. https://doi.org/10.1029/2005GL023551

Teklemariam M, Battaglia S, Gianelli G, Ruggieri G (1996) Hydrothermal alteration in the Aluto-Langano geothermal field, Ethiopia. Geothermics 25:679–702. https://doi.org/10.1016/S0375-6505(96)00019-3

Tello-López MR, Torres-Rodríguez MA, (2015) Behavior of the production characteristics of the wells in the Las Tres Vírgenes, BCS,

Geothermal Field, México. In: Proceedings world geothermal congress 2015, pp 19–25

Thomsen L (1995) Elastic anisotropy due to aligned cracks in porous rock. Geophys Prospect 43:805–829

Tosha T, Sugihara M, Nishi Y (1998) Revised hypocenter solutions for microearthquakes in the Kakkonda geothermal field Japan. Geothermics 27(5–6):553–571. https://doi.org/10.1016/S0375-6505(98)00033-9

van Der Kolk CM, Guest WS, Potters JHHM (2001) The 3D shear experiment over the Natih field in Oman, the effect of fracture-filling fluids on shear propagation. Geophys Prospect 49:179–197

Vanorio T, Virieux J, Capuano P, Russo G (2005) Three-dimensional seismic tomography from P wave and S wave microearthquake travel times and rock physics characterization of the Campi Flegrei Caldera. J Geophys Res Solid Earth. https://doi.org/10.1029/2004JB003102

Vasco DW, Ferretti A, Novali F (2008) Estimating permeability from quasi-static deformation: TEMPORAL variations and arrival-time inversion. Geophysics 73(6):O37–O52

Vilchis-García V, Calò M, Samaniego JFL (2019) Imaging of the magmatic system feeding Las Tres Virgenes Geothermal field (Baja California Sur, Mexico) using enhanced seismic tomography. J Volcanol Geoth Res 388:106710. https://doi.org/10.1016/j.jvolgeores.2019.106710

Vlahovic G, Elkibbi M, Rial JA (2002) Temporal variations of fracture directions and fracture densities in the Coso geothermal field from analyses of shear-wave splitting. In: Proceedings of the 27th workshop on geothermal reservoir engineering, Stanford University, Stanford, California (Vol. 415)

Werner U, Shapiro SA (1999) Frequency-dependent shear-wave splitting in thinly layered media with intrinsic anisotropy. Geophysics 64:604–608

Wong V, Rebollar CJ, Munguía L (2001) Attenuation of coda waves at the Tres Vírgenes volcanic area, Baja California Sur, México. Bull Seismol Soc Am 91(4):683–693

Zhao D, Mishra OP, Sanda R (2002) Influence of fluids and magma on earthquakes: seismological evidence. Phys Earth Planet Inter 132(4):249–267

Zúñiga FR, Castro RR, Domínguez T (1995) Stress orientation and anisotropy based on shear-wave splitting observations in the Cerro Prieto fault area, Baja California Mexico. Pure Appl Geophys 144(1):39–57. https://doi.org/10.1007/BF00876473